

Striatal activity topographically reflects cortical activity

<https://doi.org/10.1038/s41586-020-03166-8>

Received: 15 July 2019

Accepted: 9 December 2020

Published online: 20 January 2021

 Check for updates

Andrew J. Peters¹✉, Julie M. J. Fabre², Nicholas A. Steinmetz^{1,2,3}, Kenneth D. Harris^{2,4} & Matteo Carandini^{1,4}

The cortex projects to the dorsal striatum topographically^{1,2} to regulate behaviour^{3–5}, but spiking activity in the two structures has previously been reported to have markedly different relations to sensorimotor events^{6–9}. Here we show that the relationship between activity in the cortex and striatum is spatiotemporally precise, topographic, causal and invariant to behaviour. We simultaneously recorded activity across large regions of the cortex and across the width of the dorsal striatum in mice that performed a visually guided task. Striatal activity followed a mediolateral gradient in which behavioural correlates progressed from visual cue to response movement to reward licking. The summed activity in each part of the striatum closely and specifically mirrored activity in topographically associated cortical regions, regardless of task engagement. This relationship held for medium spiny neurons and fast-spiking interneurons, whereas the activity of tonically active neurons differed from cortical activity with stereotypical responses to sensory or reward events. Inactivation of the visual cortex abolished striatal responses to visual stimuli, supporting a causal role of cortical inputs in driving the striatum. Striatal visual responses were larger in trained mice than untrained mice, with no corresponding change in overall activity in the visual cortex. Striatal activity therefore reflects a consistent, causal and scalable topographical mapping of cortical activity.

The dorsal striatum serves several sensory^{10–12}, motor¹³ and cognitive^{14,15} roles, and receives a major synaptic input from the cortex^{16,17} that is ordered topographically^{1,2,18}. Yet, with few exceptions^{19,20} recordings have suggested marked differences in sensory and behavioural correlates between striatal and cortical neurons^{6–9} and across striatal cell types^{7,21–23}. These differences could arise from noncortical striatal inputs, including other basal ganglia nuclei²⁴ and the thalamus^{25,26}, and from local striatal circuitry²⁷. However, the possibility remains that the cortex and striatum carry similar sensorimotor signals, but that this similarity is apparent only in topographically matched regions. Indeed, functional MRI in humans showed that cortical and striatal signals measured at rest are topographically correlated²⁸.

We trained mice to turn a steering wheel to move a visual grating from the periphery to the centre²⁹ (Fig. 1a, b). The stimulus remained fixed for 500 ms, and then an auditory ‘go’ cue signalled that the stimulus position became yoked to a steering wheel and could be brought to the centre to elicit a water reward (Extended Data Fig. 1a). The correct response to a stimulus on the right (contralateral to the striatal recordings) was to turn the wheel anticlockwise, which moved the stimulus from right to centre. We refer to such movements as ‘contralaterally orienting’. Mice performed the task proficiently, often with fast reaction times that preceded the ‘go’ cue (Extended Data Fig. 1b–d).

While mice performed this task, we recorded activity simultaneously across the dorsal cortex and along a mediolateral trajectory that spanned the dorsal striatum (Fig. 1c, d). We recorded from cortical

excitatory neurons (using *CaMK2a-tTA;tetO-GCaMP6s* transgenic mice³⁰) with wide-field calcium imaging, aligning the images across sessions using vasculature and across mice using retinotopic maps (Extended Data Fig. 2). At the same time, we recorded with a Neuropixels probe³¹ along the width of the striatum ($n = 77$ sessions across 15 mice) (Fig. 1d). The probe trajectory was standardized across sessions (Extended Data Fig. 3a, b), and yielded consistent electrophysiological landmarks that delimited the striatum (Extended Data Fig. 3c, d).

Progression of task-related activity

Both the cortex and striatum displayed a progression of activity to visual stimuli, movement and licking of the reward (Fig. 1e, f). Following the visual stimulus, cortical activity was strongest in visual and frontomedial regions. At the time of movement, cortical activity spread to retrosplenial and limb somatomotor regions (primary somatosensory (SSp-II and SSp-ul) and posterior primary motor cortex (MOp)). During licking of the reward, activity shifted to orofacial somatomotor regions (SSp-m, lateral MOp and lateral secondary motor cortex (MOs)) (Fig. 1e). Echoing this flow of cortical activity, striatal activity progressed mediolaterally from visual stimulus to movement to licking (Fig. 1f).

Although the imaging was focused on the cortical surface, it reflected spikes in deep layers (Extended Data Fig. 4). In a subset of mice, we inserted a second Neuropixels probe in the visual cortex ($n = 10$ sessions

¹UCL Institute of Ophthalmology, University College London, London, UK. ²UCL Queen Square Institute of Neurology, University College London, London, UK. ³Present address: Department of Biological Structure, University of Washington, Seattle, WA, USA. ⁴These authors jointly supervised this work: Kenneth D. Harris, Matteo Carandini. ✉e-mail: peters.andrew.j@gmail.com

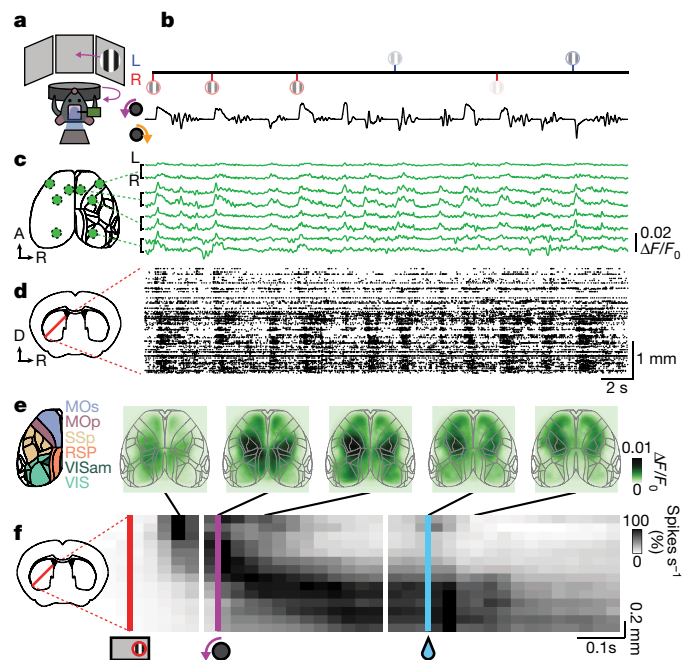


Fig. 1 | The cortex and striatum show spatial gradients of sensorimotor activity during visually guided behaviour. **a**, Cartoon of the task, showing a mouse turning a steering wheel surrounded by three screens. L, left; R, right. **b**, Timeline of task events from an example session, showing gratings of various contrasts appearing on the left or right of the mouse (top) and velocity of the steering wheel (bottom). **c**, Cortical activity measured by wide-field calcium imaging during the period in **b**. Deconvolved fluorescence traces are shown for the orofacial and limb primary motor cortex, secondary motor cortex and primary visual cortex. A, anterior. **d**, Spikes measured simultaneously across the dorsal striatum during the same period. D, dorsal. **e**, Temporally deconvolved cortical fluorescence maps, at five time points averaged across all trials of all sessions with right-hand stimuli, correct anticlockwise wheel turns and reaction times <500 ms. SSp, primary somatosensory cortex; RSP, retrosplenial cortex; VIS, visual cortex. **f**, Mean multiunit firing rate in striatum as a function of location and time, averaged over the same events as in **e**. The three grey-scale panels represent activity aligned to visual stimulus onset (red line), contralaterally orienting movements (purple line) and reward delivery (cyan line). Firing rates are arranged by distance from the lateral striatal border, averaged across sessions and maximum-normalized.

across 3 mice) and determined a deconvolution kernel that optimally predicted cortical firing from wide-field activity (Extended Data Fig. 4a, b). The deconvolved wide-field signal correlated best with spikes in deep layers (Extended Data Fig. 4c, d), perhaps owing to deep neurons having higher firing rates and superficial apical dendrites that drive fluorescence in layer 1³². Similar results were obtained with deconvolution kernels derived from only superficial or only deep spiking (Extended Data Fig. 4e).

Cortical and striatal topography

Correlations of striatal spikes at each location with cortical activity revealed an orderly progression of topographical cortical maps (Fig. 2a–e). This progression could be seen in spike-triggered averages of cortical wide-field fluorescence for successively lateral striatal locations (Fig. 2a). However, spike-triggered averaging reflects not only interactions between signals but also autocorrelations within signals. The latter are prominent during the task, as sensory and motor activity often overlapped. To correct for these autocorrelations, we predicted striatal spiking from cortical fluorescence using the best-fitting spatial kernels, which defined a precise cortical map for each striatal location (Fig. 2b). Striatal regions along a mediolateral progression were

associated with well-defined cortical regions that progressed from posterior to frontomedial to frontolateral (Fig. 2c). Their progression was continuous (Fig. 2d), but for ease of description we grouped striatal locations into three domains: dorsomedial, dorsocentral and dorsolateral (DMS, DCS, and DLS, respectively) (Fig. 2d, e). The reliable relationship of cortical and striatal activity enabled us to align striatal activity across sessions, using cortical correlations to identify striatal domains without relying on estimated coordinates.

The cortical map associated with each striatal domain was invariant to behaviour and consistent with anatomical projections (Fig. 2f–h). The cortical maps that predicted activity of the DMS, DCS and DLS during task performance focused, respectively, on the anteromedial visual area (VISam), the frontomedial MOs and the orofacial somatomotor cortex (SSp-m, lateral MOP and MOs) (Fig. 2f). Similar maps were obtained while mice passively viewed visual noise stimuli (Fig. 2g), which indicates that the relationship between cortex and striatum was invariant to behavioural context. Indeed, these functional cortical maps resembled patterns of corticostriatal projections reported by the Allen Mouse Brain Connectivity Atlas¹⁸ (Fig. 2h), which suggests that the functional relationship between cortex and striatum is primarily determined by fixed anatomical connectivity.

The relationship between striatal activity and cortical activity was stereotyped in both space and time (Fig. 2i, j). To examine the spatiotemporal association between cortical and striatal activity, we fit cortical kernels as above and allowed a lag range of –100 to 100 ms. The resulting kernels identified a unique cortical pattern for each domain that ramped up and down in time and was weighted more strongly when cortical activity led striatal activity (Fig. 2i). These kernels were similar across sessions and behavioural context, again indicating a fixed relationship in activity between the cortex and striatum (Fig. 2j).

Striatal activity correlated best with deep cortical layers, with a latency consistent with monosynaptic connections (Extended Data Fig. 4). In the three mice with an additional Neuropixels probe in VISam, we compared the associated striatal activity (in the DMS) with spiking across cortical layers ($n = 10$ sessions). Striatal activity correlated best with cortical spiking in deep layers (Extended Data Fig. 4c–f), consistent with the laminar position of corticostriatal neurons³³. Given that cortical fluorescence also correlated best with spikes in deep cortical layers, these findings suggest that corticostriatal neurons in deep cortical layers drive the relationship between wide-field cortical activity and striatal spikes (Extended Data Fig. 4d). Consistent with this hypothesis, spiking activity in the deep layers of VISam led spiking in the DMS by about 3 ms, similar to measurements of corticostriatal lag⁹ (Extended Data Fig. 4f).

Striatum and cortex share task responses

Firing rates in the three striatal domains reflected three task events: contralateral stimuli in the DMS, contralaterally orienting movements in the DCS and reward licking in the DLS (Fig. 3a). Ipsilateral stimuli did not evoke activity, and ipsilateral movements elicited less activity than contralateral movements (Extended Data Fig. 5a). Visual responses in the DMS depended on stimulus contrast but not on the upcoming choice of the mouse, which indicates that they encode sensory stimuli rather than action plans (Extended Data Fig. 6a). The auditory ‘go’ cue elicited activity in the DMS only if mice had not already begun turning the wheel (Fig. 3a, Extended Data Fig. 6b, c).

Firing rates in the three striatal domains were faithfully predicted from task events (Fig. 3b, c). To isolate the striatal correlates of individual task events, we fit striatal spiking as a sum of event kernels triggered on the times of stimuli of each contrast, movements in either direction, the ‘go’ cue, and rewarded and unrewarded outcomes. These event kernels described contrast-dependent contralateral stimulus responses mostly in the DMS, contralaterally biased movement responses in the DCS and reward-licking responses in the DLS

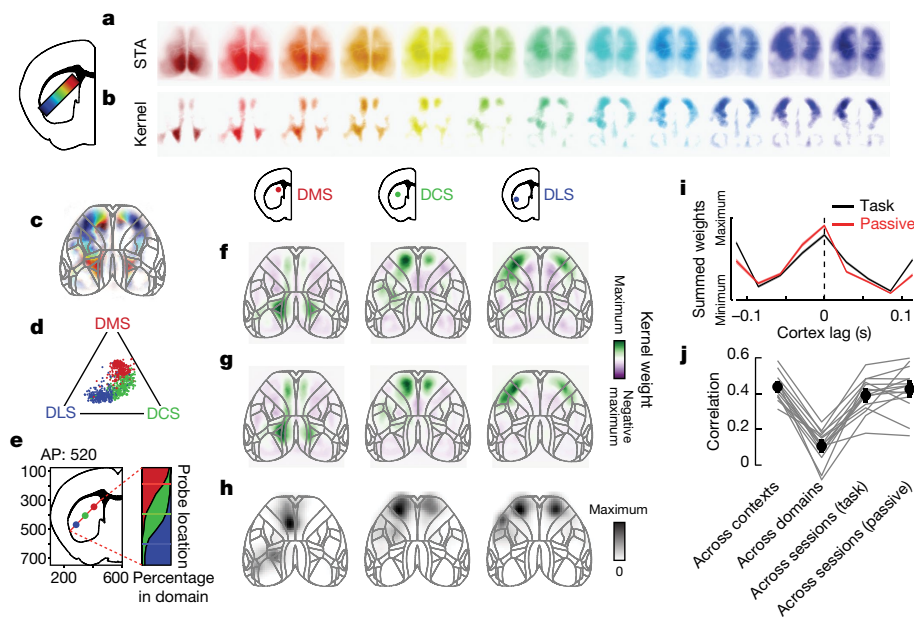


Fig. 2 | Striatal domains are topographically correlated with connected cortical regions. **a**, Spike-triggered average (STA) of deconvolved cortical fluorescence for multiunit activity at each striatal location (indexed by colours), averaged across sessions from all mice. **b**, Regressed spatial kernels corresponding to locations in **a**. **c**, Striatal depth corresponding to centre-of-mass kernel weights for each cortical pixel, using the same colour scale as **a**. **d**, Ternary plot showing relative correlation of the cortical kernels for each 200- μ m striatal segment in each session (dots) with the 3 template kernels used to assign each segment to a striatal domain (vertices). **e**, Left, centre-of-mass common coordinate framework (CCF) location for each striatal domain estimated from all striatal segments in **d**. Right, cumulative fraction of striatal segments in **d** categorized into each domain relative to CCF location. AP, anterior–posterior coordinate. **f**, Mean cortical spatial kernels for each striatal domain (lag = 0 s) during the task, averaged across sessions and

maximum-normalized. **g**, Cortical spatial kernels as in **f** computed while mice passively viewed visual noise stimuli. **h**, Density of cortical locations projecting to each striatal domain, data from the Allen Mouse Brain Connectivity Atlas¹⁸. **i**, Time course of spatially summed cortical kernel weights, measured in the behavioural task (black) or during passive viewing of visual noise (red). Curves show mean across domains and sessions \pm s.e. across sessions. The kernel weights are larger for the cortex leading striatum (signed-rank test, $P = 2.5 \times 10^{-6}$ across 77 sessions). **j**, Correlation of spatiotemporal cortical kernels across contexts (task versus passive), across striatal domains and across sessions (mean \pm s.e. across mice). Cortical kernels fit from different domains are significantly less correlated than kernels from different behavioural contexts or recording sessions (signed-rank test, $P = 6.1 \times 10^{-5}$ across 15 mice).

(Fig. 3b, Extended Data Fig. 6b, c). Together, these event kernels were sufficient to predict trial-by-trial striatal activity (Fig. 3c, Extended Data Fig. 5b) (cross-validated $R^2 = 0.12 \pm 0.01$ in the DMS, 0.35 ± 0.02 in the DCS and 0.45 ± 0.02 in the DLS (mean \pm s.e. across sessions)).

Notably, firing rates in the three striatal domains could be predicted from cortical activity despite no explicit inclusion of task events (Fig. 3d–f). We predicted firing rates in each striatal domain by applying the domain's unique spatiotemporal kernel to cortical activity (Fig. 3d). This prediction was accurate (Fig. 3a, d, e), describing trial-by-trial striatal activity as well or better than predictions from task events (Fig. 3f) (cross-validated $R^2 = 0.17 \pm 0.02$ in the DMS, 0.33 ± 0.03 in the DCS and 0.44 ± 0.02 in the DLS (mean \pm s.e. across sessions)). Cortical activity was an accurate predictor of striatal activity because striatal domains and their associated cortical regions had essentially identical sensorimotor correlates (Extended Data Fig. 7a–c), which explained consistent fractions of variance across the two structures (Extended Data Fig. 7d). Good predictions of striatal firing were only possible from the associated cortical regions of a domain, and not from other cortical regions or other striatal domains (Extended Data Fig. 8a).

Striatal activity topographically mirrored the associated cortical regions not only during the sensorimotor task, but also while mice were passive outside the task (Extended Data Fig. 8b–e). When mice passively viewed visual noise stimuli, the visual cortex and DMS exhibited oscillating, synchronous activity³⁴, whereas the DCS and DLS were less active owing to reduced movement (Extended Data Fig. 8b). Despite these contextual differences in striatal activity, cortical activity predicted striatal firing as well as during task performance, explaining slightly

more variance in the DMS and slightly less in the DCS and DLS (Extended Data Fig. 8c). These slight differences were consistent with the changes in variance between task and rest (Extended Data Fig. 8d), suggesting that the amount of striatal activity explained by cortex was determined by the amount of signal present to explain (Extended Data Fig. 8e).

The close match between cortical and striatal activity suggests that the striatum inherits its task responses from the cortex, a hypothesis that was supported by inactivation experiments (Fig. 3g, Extended Data Fig. 9). In six of the mice, we performed our simultaneous cortical and striatal measurements before and after inactivation of VISam with topical muscimol. Cortical muscimol effectively silenced spiking in all layers of cortex (Extended Data Fig. 9a). When applied over VISam, it strongly reduced local visual responses (Extended Data Fig. 9b). Cortical muscimol slightly increased the average striatal firing rate (Extended Data Fig. 9c), but reduced visual responses in the DMS (Fig. 3g) proportionally to the reduction in VISam (Extended Data Fig. 9d). During task performance, cortical muscimol increased reaction times and increased contralaterally orienting responses particularly at low ipsilateral contrasts, which suggests that mice used only the ipsilateral stimuli to guide movements and defaulted to the contralateral side when the ipsilateral stimulus was not perceived (Extended Data Fig. 9e). Fitting task-event kernels to neural activity revealed that inactivation of VISam selectively eliminated striatal visual responses, and spared activity related to movement and reward licking (Extended Data Fig. 9f). These results indicate that—at least for visual responses—striatal firing requires the propagation of activity from the associated cortical region.

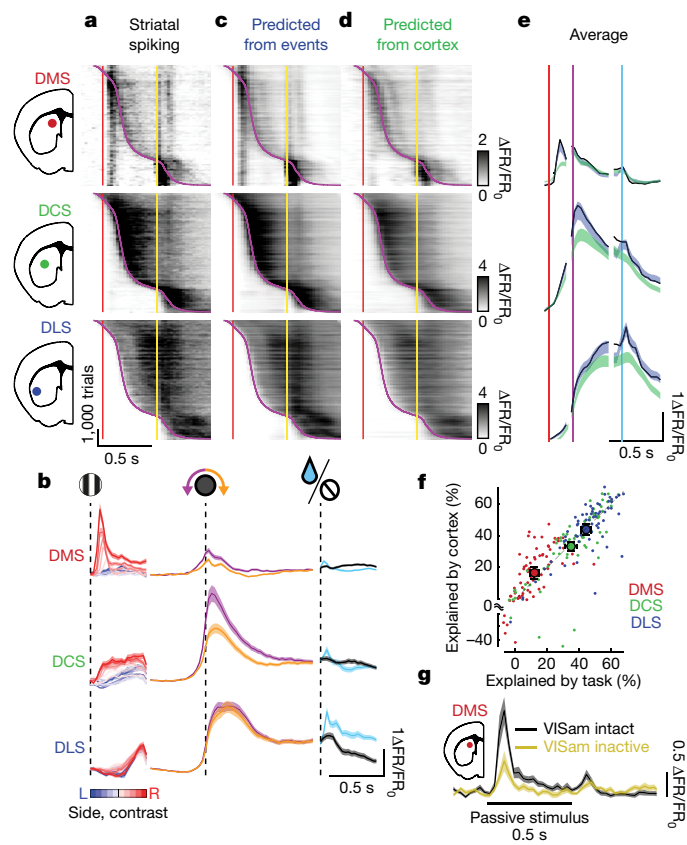


Fig. 3 | Striatal sensorimotor activity reflects associated cortical activity. **a**, Multiunit activity in each striatal domain, shown for all trials with contralateral stimuli, contralaterally orienting movements, and rewards. Trials are aligned by stimulus onset (red line), which was followed 500 ms later by a 'go' cue (yellow line). Trials are combined across sessions and sorted by reaction time (time of movement onset (purple curve)). For graphical purposes, activity at each time is smoothed with a running average of 100 trials to highlight features that are consistent across trials. FR, firing rate. **b**, Event kernels predicting activity in each striatal domain from task events. Left column, kernels for ipsilateral (blue) and contralateral (red) stimuli of different contrasts (colour saturation). Middle column, kernels for contralateral-orienting (purple) and ipsilateral-orienting (orange) movements. Right column, kernels for reward delivery on correct trials (cyan) and white noise on incorrect trials (black). Vertical black dotted lines indicate event onset, shading indicates mean \pm s.e. across sessions. **c**, Prediction of striatal firing rate obtained from task events, formatted as in **a**. **d**, Prediction of striatal firing rate from cortical activity, formatted as in **a**. **e**, Trial-averaged activity in each striatal domain (black), predicted from task events (blue) and predicted from cortical activity (green), aligned to stimulus (red line), movement (purple line) and reward delivery (cyan line) (mean \pm s.e. across sessions). **f**, Cross-validated explained variance (R^2) of striatal activity predicted from the cortex and task. Small dots, sessions; large dots, mean \pm s.e. across sessions; colour, striatal domain. The cortex explains more or the same amount of striatal activity as task events, indicating that striatal activity mirrors cortical activity (signed-rank test, DMS $P = 5.8 \times 10^{-4}$, DCS $P = 0.17$, DLS $P = 0.48$). **g**, Passive responses to visual stimuli in the DMS before (black) and after (yellow) inactivation of VISam with muscimol.

Striatal cell type activity

The match between activity in the striatum and topographically associated cortex held for putative medium spiny neurons (MSNs) and putative parvalbumin-positive³⁵ fast-spiking interneurons (FSIs), but not for putative cholinergic³⁶ tonically active neurons (TANs), which had responses that were notably different and stereotyped (Fig. 4a–c). MSNs constitute 95% of striatal neurons; the rest are interneurons that have been proposed to have unique responses^{7,21,22}. To examine the

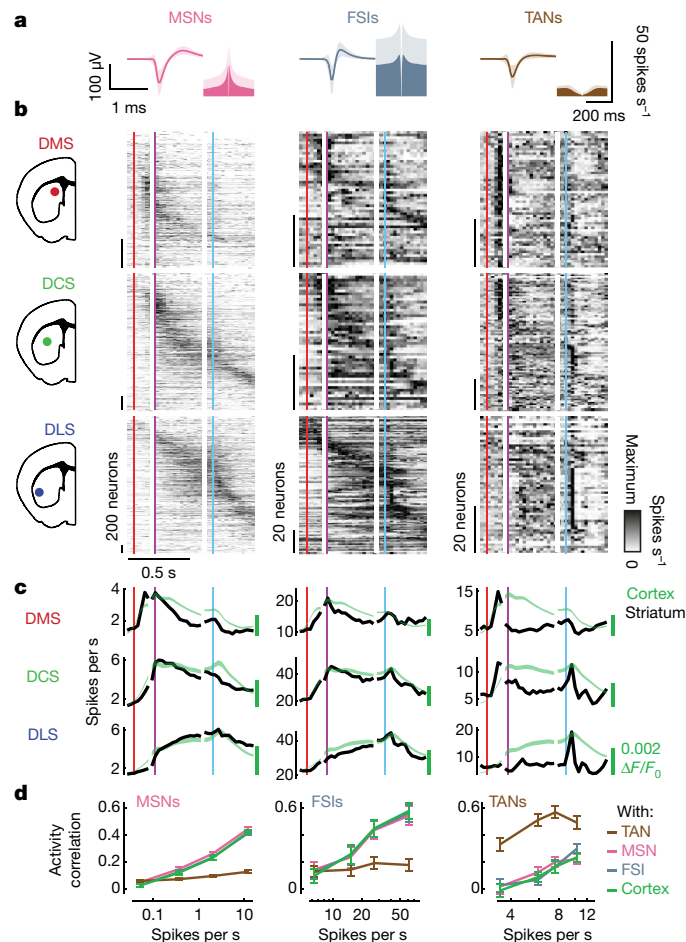


Fig. 4 | Striatal mirroring of cortical activity is cell-type-specific. **a**, Spike waveforms and autocorrelograms for striatal MSNs, FSIs and TANs (mean \pm s.d. across cells). **b**, Heat maps showing firing rates of individual cells of each class aligned to contralateral stimuli (red lines), contralaterally orienting movements (purple lines) and rewards (blue lines), averaged across trials with reaction times < 500 ms, maximum-normalized and sorted by time of maximum activity using half of the trials and plotting the other half of trials. Rows correspond to striatal domains (the DMS, DCS and DLS) and columns correspond to cell types. **c**, Activity as in **b**, averaged across neurons of each cell type and domain (black). For reference, each row reports the cortical activity within a region of cortex associated with each domain (green), providing a close match with MSN and FSI activity but not with TAN activity. **d**, Mean correlation of individual neurons with the mean activity of each cell type in the same striatal domain (black curves in **c**) or with activity of the topographically associated cortical region of interest (green curves in **c**) from nonoverlapping sessions to account for interneuron sparsity (mean \pm s.e. across sessions). MSNs and FSIs were equally correlated with themselves as with each other (shuffling MSN and FSI labels within sessions; MSN, $P = 0.47$; FSI, $P = 0.99$ across 77 sessions) or with cortical activity (two-way analysis of variance (ANOVA) on firing rate and type; type MSN, $P = 0.94$; FSI, $P = 0.88$ across 77 sessions). TANs were correlated with themselves and equally uncorrelated to MSNs, FSIs and cortical activity (two-way ANOVA on firing rate and type; TAN versus MSN, $P = 7.5 \times 10^{-48}$; TAN versus FSI, $P = 2.0 \times 10^{-6}$; TAN versus MSN, FSI and cortex, $P = 0.68$ across 77 sessions).

task-related activity of striatal neurons, we selected high-quality single units (8,303 out of 21,047) and used electrophysiological criteria^{37,38} to group them into MSNs, FSIs and TANs (Fig. 4a), plus a separate class of unidentified interneurons³⁷ (Extended Data Fig. 10). MSNs fired at a range of times associated with stimulus, movement and reward licking (Fig. 4b left). The proportion of cells responding to these events differed across domains: nearly all stimulus-responsive cells were in

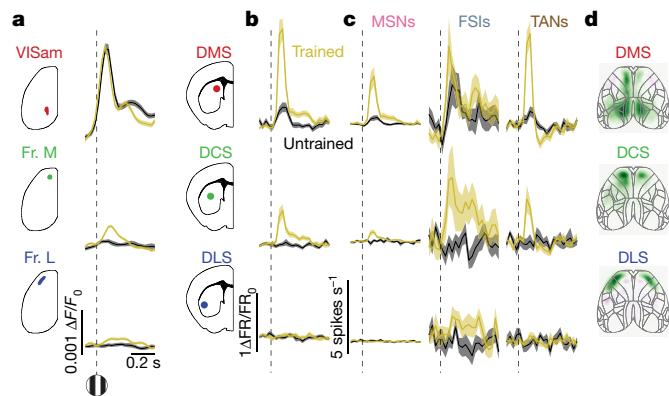


Fig. 5 | Striatal stimulus responses increase independently from visual cortex after training. **a**, Cortical activity (fluorescence) within regions associated with each striatal domain in untrained (black) and trained (yellow) mice to 100% contrast contralateral stimuli (mean \pm s.e. across sessions). Stimulus responses in VISam do not change with training; they increase in the frontomedial cortex (Fr. M) and are not present in frontolateral cortex (Fr. L) (rank-sum test; VISam, $P=0.08$; Fr. M, $P=6.2 \times 10^{-3}$ across 23 untrained and 48 trained sessions, time window 0–0.2 s). **b**, Striatal multiunit activity, plotted as in **a**. Stimulus responses increase in the DMS and DCS (rank-sum test; DMS, $P=2.1 \times 10^{-4}$; DCS, $P=9.7 \times 10^{-4}$, time window 0–0.2 s). **c**, Striatal activity as in **a** within each cell type. Stimulus responses within the DMS increases for MSNs and TANs but not for FSIs (rank-sum test; DMS, MSN $P=2.8 \times 10^{-3}$; FSI, $P=0.32$; TAN, $P=0.013$, time window 0–0.2 s). **d**, Cortical kernels for each striatal domain computed from untrained mice passively viewing visual noise (as in Fig. 2g). Average domain kernels for each mouse are equally correlated across trained mice as they are between trained and untrained mice (rank-sum test $P=0.65$).

the DMS, most movement-onset-responsive cells in the DCS and most licking-responsive cells in the DLS. Averaging MSN activity in each domain yielded a multiunit signal that mirrored activity in the topographically associated regions of cortex (Fig. 4c left). In contrast to previous reports^{7,22,39}, FSI activity resembled that of MSNs—albeit with higher firing rates (Fig. 4b, c, centre). By contrast, TANs had different activity: they responded synchronously with a burst followed by a pause following the stimulus (in the DMS and DCS) or reward licking (in the DCS and DLS), respecting an unexpected^{40,41} segregation according to striatal domain (Fig. 4b, c, right).

These results suggest that whereas MSNs and FSIs are similarly driven by cortical activity, TANs are more independent, consistent with their weaker cortical input⁴² (Fig. 4d). To quantify these effects, we correlated the activity of individual striatal neurons with the summed activity of each cell type in their domain, and with cortical wide field in the associated region. MSNs and FSIs showed similar correlation with the activity of either class and with topographical cortical activity, but a low correlation with TAN activity (Fig. 4d left and centre). By contrast, TAN activity correlated strongly with other TANs but weakly with other cell types or with cortex (Fig. 4d right).

Training striatal sensory responses

Training in the task increased DMS sensory responses in both MSNs and TANs, but not in FSIs (Fig. 5). We compared responses to visual stimuli in untrained mice ($n=23$ sessions, 5 mice) and in trained mice while in a passive context ($n=48$ sessions in 11 mice), excluding trials with wheel movements. Cortical responses in VISam were similar in untrained and trained mice (Fig. 5a). By contrast, trained mice had larger visual responses in the DMS (Fig. 5b). This increase affected MSNs and TANs but not FSIs, which indicates a differential effect of training across cell types (Fig. 5c). Training also gave rise to stimulus responses in the DCS (Fig. 5b, c), which were probably inherited from

training-induced stimulus responses in the associated frontomedial cortex⁴³ (Fig. 5a centre). Nonetheless, cortical kernels for each striatal domain had a consistent topography and time course across trained and untrained mice (Fig. 5d). This indicates that the spatiotemporal relationship between the cortex and striatum is consistent, with a gain that changes across learning.

Discussion

These results establish that summed activity in each striatal domain causally reflects summed activity in the topographically associated cortical region, independent of behavioural context but scaled by learning. These results contrast with those of previous studies, which have suggested marked differences between cortical and striatal activity^{6–8} and between MSN and FSI activity^{7,22}, possibly owing to the difficulty in precisely matching associated cortical and striatal regions and consistently recording in the same striatal locations.

Our data suggest that associated regions of cortex and basal ganglia form a continuously cooperative circuit that is active throughout sensation and movement rather than just at event onsets and offsets⁴⁴. This circuit may link stimuli to actions^{5,15} and continuously modulate behaviour^{13,20,39}. Striatal activity is also likely to reflect noncortical inputs from the amygdala, hippocampus and thalamus². Indeed, the thalamus provides almost half of all excitatory synapses to the striatum¹⁷ and dominates the inputs to TANs⁴², potentially explaining their difference from cortical activity.

Our data also indicate that although the overall transfer function from the cortex to the striatum is stable, its gain is scalable with learning. This gain change operates at the level of summed activity; individual MSNs showed diverse activity correlates, and their learning-related plasticity may also be diverse, and perhaps differ across direct and indirect MSNs⁴⁵. Our results are consistent with previous reports that learning strengthens corticostriatal synapses^{45–47} and correlations^{20,48}, and suggest that cortical activity may most effectively propagate to the striatum when it has been learned as behaviourally relevant. Notably, no gain change was seen in FSIs, which suggests that these neurons regulate MSN activity⁴⁹ independently of learning.

Overall, there is a close relationship between cortical and striatal activity, which is largely determined by topography and invariant to context. Cortical signals are faithfully reflected in striatum, and are therefore poised to determine further processing as activity propagates through the basal ganglia to determine behaviour.

Online content

Any methods, additional references, Nature Research reporting summaries, source data, extended data, supplementary information, acknowledgements, peer review information; details of author contributions and competing interests; and statements of data and code availability are available at <https://doi.org/10.1038/s41586-020-03166-8>.

1. Hintiryan, H. et al. The mouse cortico-striatal projectome. *Nat. Neurosci.* **19**, 1100–1114 (2016).
2. Hunnicutt, B. J. et al. A comprehensive excitatory input map of the striatum reveals novel functional organization. *eLife* **5**, e19103 (2016).
3. Friedman, A. et al. A corticostriatal path targeting striosomes controls decision-making under conflict. *Cell* **161**, 1320–1333 (2015).
4. Gremel, C. M. et al. Endocannabinoid modulation of orbitostriatal circuits gates habit formation. *Neuron* **90**, 1312–1324 (2016).
5. Znamenskiy, P. & Zador, A. M. Corticostriatal neurons in auditory cortex drive decisions during auditory discrimination. *Nature* **497**, 482–485 (2013).
6. Fujii, N. & Graybiel, A. M. Time-varying covariance of neural activities recorded in striatum and frontal cortex as monkeys perform sequential-saccade tasks. *Proc. Natl Acad. Sci. USA* **102**, 9032–9037 (2005).
7. Martiros, N., Burgess, A. A. & Graybiel, A. M. Inversely active striatal projection neurons and interneurons selectively delimit useful behavioral sequences. *Curr. Biol.* **28**, 560–573. e5 (2018).
8. Buch, E. R., Brasted, P. J. & Wise, S. P. Comparison of population activity in the dorsal premotor cortex and putamen during the learning of arbitrary visuomotor mappings. *Exp. Brain Res.* **169**, 69–84 (2006).

9. Pidoux, M., Mahon, S., Deniau, J. M. & Charpier, S. Integration and propagation of somatosensory responses in the corticostriatal pathway: an intracellular study in vivo. *J. Physiol. (Lond.)* **589**, 263–281 (2011).
10. Kim, H. F. & Hikosaka, O. Distinct basal ganglia circuits controlling behaviors guided by flexible and stable values. *Neuron* **79**, 1001–1010 (2013).
11. Wang, L., Rangarajan, K. V., Gerfen, C. R. & Krauzlis, R. J. Activation of striatal neurons causes a perceptual decision bias during visual change detection in mice. *Neuron* **97**, 1369–1381.e5 (2018).
12. Guo, L., Walker, W. I., Ponvert, N. D., Penix, P. L. & Jaramillo, S. Stable representation of sounds in the posterior striatum during flexible auditory decisions. *Nat. Commun.* **9**, 1534 (2018).
13. Rueda-Orozco, P. E. & Robbe, D. The striatum multiplexes contextual and kinematic information to constrain motor habits execution. *Nat. Neurosci.* **18**, 453–460 (2015).
14. Tai, L.-H., Lee, A. M., Benavidez, N., Bonci, A. & Wilbrecht, L. Transient stimulation of distinct subpopulations of striatal neurons mimics changes in action value. *Nat. Neurosci.* **15**, 1281–1289 (2012).
15. Yartsev, M. M., Hanks, T. D., Yoon, A. M. & Brody, C. D. Causal contribution and dynamical encoding in the striatum during evidence accumulation. *eLife* **7**, e34929 (2018).
16. Kincaid, A. E., Zheng, T. & Wilson, C. J. Connectivity and convergence of single corticostriatal axons. *J. Neurosci.* **18**, 4722–4731 (1998).
17. Huerta-Ocampo, I., Mena-Segovia, J. & Bolam, J. P. Convergence of cortical and thalamic input to direct and indirect pathway medium spiny neurons in the striatum. *Brain Struct. Funct.* **219**, 1787–1800 (2014).
18. Oh, S. W. et al. A mesoscale connectome of the mouse brain. *Nature* **508**, 207–214 (2014).
19. Emmons, E. B. et al. Rodent medial frontal control of temporal processing in the dorsomedial striatum. *J. Neurosci.* **37**, 8718–8733 (2017).
20. Lemke, S. M., Ramanathan, D. S., Guo, L., Won, S. J. & Ganguly, K. Emergent modular neural control drives coordinated motor actions. *Nat. Neurosci.* **22**, 1122–1131 (2019).
21. Apicella, P. Tonicly active neurons in the primate striatum and their role in the processing of information about motivationally relevant events. *Eur. J. Neurosci.* **16**, 2017–2026 (2002).
22. Gage, G. J., Stoetznner, C. R., Wiltschko, A. B. & Berke, J. D. Selective activation of striatal fast-spiking interneurons during choice execution. *Neuron* **67**, 466–479 (2010).
23. Stalnaker, T. A., Berg, B., Aujla, N. & Schoenbaum, G. Cholinergic interneurons use orbitofrontal input to track beliefs about current state. *J. Neurosci.* **36**, 6242–6257 (2016).
24. Bolam, J. P., Hanley, J. J., Booth, P. A. C. & Bevan, M. D. Synaptic organisation of the basal ganglia. *J. Anat.* **196**, 527–542 (2000).
25. Kato, S. et al. Selective neural pathway targeting reveals key roles of thalamostriatal projection in the control of visual discrimination. *J. Neurosci.* **31**, 17169–17179 (2011).
26. Ponvert, N. D. & Jaramillo, S. Auditory thalamostriatal and corticostriatal pathways convey complementary information about sound features. *J. Neurosci.* **39**, 271–280 (2019).
27. Burke, D. A., Rotstein, H. G. & Alvarez, V. A. Striatal local circuitry: a new framework for lateral inhibition. *Neuron* **96**, 267–284 (2017).
28. Choi, E. Y., Yeo, B. T. T. & Buckner, R. L. The organization of the human striatum estimated by intrinsic functional connectivity. *J. Neurophysiol.* **108**, 2242–2263 (2012).
29. Burgess, C. P. et al. High-yield methods for accurate two-alternative visual psychophysics in head-fixed mice. *Cell Rep.* **20**, 2513–2524 (2017).
30. Wekselblatt, J. B., Fliester, E. D., Piscopo, D. M. & Niell, C. M. Large-scale imaging of cortical dynamics during sensory perception and behavior. *J. Neurophysiol.* **115**, 2852–2866 (2016).
31. Jun, J. J. et al. Fully integrated silicon probes for high-density recording of neural activity. *Nature* **551**, 232–236 (2017).
32. Allen, W. E. et al. Global representations of goal-directed behavior in distinct cell types of mouse neocortex. *Neuron* **94**, 891–907.e6 (2017).
33. Shepherd, G. M. G. Corticostriatal connectivity and its role in disease. *Nat. Rev. Neurosci.* **14**, 278–291 (2013).
34. Senzai, Y., Fernandez-Ruiz, A. & Buzsáki, G. Layer-specific physiological features and interlaminar interactions in the primary visual cortex of the mouse. *Neuron* **101**, 500–513.e5 (2019).
35. Mallet, N., Le Moine, C., Charpier, S. & Gonon, F. Feedforward inhibition of projection neurons by fast-spiking GABA interneurons in the rat striatum in vivo. *J. Neurosci.* **25**, 3857–3869 (2005).
36. Inokawa, H., Yamada, H., Matsumoto, N., Muranishi, M. & Kimura, M. Juxtacellular labeling of tonically active neurons and phasically active neurons in the rat striatum. *Neuroscience* **168**, 395–404 (2010).
37. Yamin, H. G., Stern, E. A. & Cohen, D. Parallel processing of environmental recognition and locomotion in the mouse striatum. *J. Neurosci.* **33**, 473–484 (2013).
38. Schmitzer-Torbert, N. C. & Redish, A. D. Task-dependent encoding of space and events by striatal neurons is dependent on neural subtype. *Neuroscience* **153**, 349–360 (2008).
39. Kim, N. et al. A striatal interneuron circuit for continuous target pursuit. *Nat. Commun.* **10**, 2715 (2019).
40. Benhamou, L., Kehat, O. & Cohen, D. Firing pattern characteristics of tonically active neurons in rat striatum: context dependent or species divergent? *J. Neurosci.* **34**, 2299–2304 (2014).
41. Marche, K., Martel, A.-C. & Apicella, P. Differences between dorsal and ventral striatum in the sensitivity of tonically active neurons to rewarding events. *Front. Syst. Neurosci.* **11**, 52 (2017).
42. Johansson, Y. & Silberberg, G. The functional organization of cortical and thalamic inputs onto five types of striatal neurons is determined by source and target cell identities. *Cell Rep.* **30**, 1178–1194.e3 (2020).
43. Orsolic, I., Rio, M., Mrcsic-Flogel, T. D. & Znamenskiy, P. Mesoscale cortical dynamics reflect the interaction of sensory evidence and temporal expectation during perceptual decision-making. Preprint at <https://doi.org/10.1101/552026> (2019).
44. Sales-Carbonell, C. et al. No discrete start/stop signals in the dorsal striatum of mice performing a learned action. *Curr. Biol.* **28**, 3044–3055.e5 (2018).
45. Rothwell, P. E. et al. Input- and output-specific regulation of serial order performance by corticostriatal circuits. *Neuron* **88**, 345–356 (2015).
46. O’Hare, J. K. et al. Pathway-specific striatal substrates for habitual behavior. *Neuron* **89**, 472–479 (2016).
47. Xiong, Q., Znamenskiy, P. & Zador, A. M. Selective corticostriatal plasticity during acquisition of an auditory discrimination task. *Nature* **521**, 348–351 (2015).
48. Koralek, A. C., Costa, R. M. & Carmena, J. M. Temporally precise cell-specific coherence develops in corticostriatal networks during learning. *Neuron* **79**, 865–872 (2013).
49. Owen, S. F., Berke, J. D. & Kreitzer, A. C. Fast-spiking interneurons supply feedforward control of bursting, calcium, and plasticity for efficient learning. *Cell* **172**, 683–695.e15 (2018).

Publisher’s note Springer Nature remains neutral with regard to jurisdictional claims in published maps and institutional affiliations.

© The Author(s), under exclusive licence to Springer Nature Limited 2021

Article

Methods

The experiments were not randomized, and investigators were not masked to allocation during experiments and outcome assessment. No statistical methods were used to predetermine sample size.

All experiments were conducted according to the UK Animals (Scientific Procedures) Act 1986 under personal and project licences issued by the Home Office.

Mice

Mice were adult (6 weeks or older) male and female transgenic mice (*CaMK2a-tTA;tetO-GCaMP6s*³⁰) that did not show evidence of epileptiform activity⁵⁰.

Surgery

Two surgeries were performed for each mouse, the first for head-plate implantation and wide-field imaging preparation, and the second for a craniotomy for acute electrophysiology. Mice were anaesthetized with isoflurane, injected subcutaneously with carprofen and placed in a stereotaxic apparatus on a heat pad. The head was then shaved, the scalp cleaned with iodine and alcohol, and the scalp was removed to expose the skull. The cut skin was sealed with VetBond (World Precision Instruments), the skull was scraped clean and a custom head plate was fixed to the interparietal bone with dental cement (Super-Bond C&B). A plastic 3D-printed U-shaped well was then cemented to enclose the edges of the exposed skull. A layer of VetBond or Zap-A-Gap (Pacer Technology) was applied to the skull followed by two layers of UV-curing optical glue (Norland Optical Adhesives no. 81, Norland Products). Carprofen was added to the drinking water for three days after surgery. For electrophysiological recordings, on the first day of recording mice were anaesthetized and a 1-mm craniotomy was drilled or cut with biopsy punch approximately 200 μm anterior and 1,000 μm lateral to bregma. The craniotomy was then covered with Kwik-Cast (World Precision Instruments) and mice were given hours to recover before recording. Craniotomies were covered with Kwik-Cast between days.

Visually guided wheel-turning task

The task has previously been described in detail²⁹. It was programmed in Signals, part of the Rigbox MATLAB package⁵¹. Mice were trained on a two-alternative forced-choice task requiring directional forelimb movements to visual stimuli (Fig. 1, Extended Data Fig. 1a). Mice were head-fixed and rested their body and hindpaws on a stable platform and their forepaws on a wheel that was rotatable to the left and right. Trials began with 0.5 s of enforced quiescence, during which any wheel movements reset the time. A static vertical grating stimulus then appeared 90° from centre with a Gaussian window $\sigma = 20^\circ$, spatial frequency 1/15 cycles per degree, and grating phase randomly selected on each trial. After 0.5 s from stimulus onset, a 'go' cue tone (12 kHz for 100 ms) sounded and the position of the stimulus became yoked to the wheel position (for example, leftward turns moved the stimulus leftward). Mice usually began turning the wheel before the cue even on trials with 0% contrast (invisible) stimuli (Extended Data Fig. 1c), indicating a rapid decision process and expected stimulus time, although as the session progressed and mice became satiated they began waiting for the cue more often (Extended Data Fig. 1d). Bringing the stimulus to the centre (correct response) locked the stimulus in the centre for 1 s and 2 μl of water was delivered from a water spout near the mouth of the mouse, after which the stimulus disappeared and the trial ended. Alternatively, moving the stimulus 90° outward (incorrect response) locked the stimulus in place off-screen and a low burst of white noise played for 2 s, after which the trial ended. The stimulus contrast varied across trials taking the values of 0%, 6%, 12.5%, 25%, 50% or 100%. Difficulty was modulated with an alternating staircase design, in which even trials used a random contrast and odd trials followed a staircase that moved to a lower contrast after three correct responses and moved

to higher contrast after one incorrect response. Correct responses on high-contrast trials were encouraged by immediately repeating all incorrect trials with 50% or 100% contrast, but these repeated trials were excluded from all analyses. Other than repeat trials, stimulus side was selected randomly on each trial. Mice were trained in stages, in which first they were trained to about 70% performance with only 100% and 50% contrast trials, then lower contrasts were progressively and automatically added as performance increased. Imaging sessions began after all contrasts had been added, and simultaneous imaging and electrophysiology sessions began after around four days of imaging-only sessions.

Wide-field imaging and fluorescence processing

Wide-field imaging was conducted with a sCMOS camera (PCO Edge 5.5) affixed to a microscope (Scimedia THT-FLSP) with a 1.0 \times condenser lens and 0.63 \times objective lens (Leica). Images were collected with Camera 4 (PCO) and binned in 2 \times 2 blocks giving a spatial resolution of 20.6 μm per pixel at 70 Hz. Illumination was generated using a Cairn OptoLED with alternating blue (470 nm, excitation filter ET470/40 \times) and violet (405 nm, excitation filter ET405/20 \times) light to capture GCaMP calcium-dependent fluorescence and calcium-invariant haemodynamic occlusion, respectively, at 35 Hz per light source. Illumination and camera exposure were triggered externally (PCIe-6323, National Instruments) to be on for 6.5 ms including a 1-ms illumination ramp up and down time to reduce light-induced artefacts on the Neuropixels probe. Excitation light was sent through the objective with a 3-mm core liquid light guide and dichroic (387/11 single-band band pass) and emitted light was filtered (525/50-55) before the camera.

To reduce data size for storage and ease of computation, wide-field data were compressed using singular value decomposition (SVD) of the form $\mathbf{F} = \mathbf{U}\mathbf{S}\mathbf{V}^T$. The input to the SVD algorithm was \mathbf{F} , the pixels \times time matrix of fluorescence values input to the SVD algorithm; the outputs were \mathbf{U} , the pixels \times components matrix of template images; \mathbf{V} , the time \times components matrix of component time courses; and \mathbf{S} the diagonal matrix of singular values. The top 2,000 components were retained, and all orthogonally invariant operations (such as deconvolution, event-triggered averaging and ridge regression to predict striatal activity from the wide-field signal) were carried out directly on the matrix $\mathbf{S}^* \mathbf{V}$, allowing a substantial saving of time and memory.

Haemodynamic effects on fluorescence were removed by regressing out the calcium-independent signal obtained with violet illumination from the calcium-dependent signal obtained with blue illumination. To do this, both signals were band-pass filtered in the range 7–13 Hz (heart-beat frequency, expected to have the largest haemodynamic effect), downsampling the spatial components threefold and reconstructing the fluorescence for each downsampled pixel. Pixel traces for blue illumination were then temporally resampled to be concurrent with violet illumination (as colours were alternated), and a scaling factor was fit across colours for each pixel. The scaled violet traces were then subtracted from the blue traces.

To correct for slow drift, haemodynamic-corrected fluorescence was then linearly detrended, high-pass filtered over 0.01 Hz and $\Delta F/F_0$ -normalized by dividing by the average fluorescence at each pixel softened by adding the median average fluorescence across pixels.

Wide-field images across days for each mouse were aligned by rigid registration of each day's average violet-illumination image that was dominated by vasculature (Extended Data Fig. 2a). Wide-field images across mice were aligned by affine alignment of average visual field sign maps for each mouse (Extended Data Fig. 2b, c). The Allen Common Coordinate Framework⁵² (CCF v.3, © 2015 Allen Institute for Brain Science; available from: http://download.alleninstitute.org/informatics-archive/current-release/mouse_ccf) atlas was aligned to the grand average and symmetrized sign map across mice by assigning expected visual field sign to visual areas⁵³ and affine aligning the annotated CCF to the average sign map (Extended Data Fig. 2d).

Even though CCF alignment was done using posterior visual areas, it was successful in aligning the entire brain as evidenced by correspondence between correlated wide-field regions and CCF borders (Extended Data Fig. 2e, f) and the ability to accurately estimate anterior probe trajectories from wide-field images (Extended Data Fig. 3a).

To combine SVD-compressed wide-field data across recordings, data were recast from experiment-specific SVD components into a master SVD basis set. These master SVD components were created by aligning and concatenating components \mathbf{U} from the last imaging-only session of all mice (that is, no craniotomy), performing an SVD on that concatenated matrix and retaining the top 2,000 components to serve as the master SVD components. Temporal components ($\mathbf{S}^*\mathbf{V}$) for each experiment were recast by

$$\mathbf{S}^*\mathbf{V}_{\text{master}} = \mathbf{U}_{\text{master}}^T * \mathbf{U}_{\text{experiment}} * \mathbf{S}^*\mathbf{V}_{\text{experiment}}$$

Fluorescence was deconvolved using a kernel fit from predicting cortical multiunit activity from wide-field GCaMP6s fluorescence. This kernel was estimated using data from simultaneous wide-field imaging and Neuropixels recordings in the visual cortex (Extended Data Fig. 4a-b, with the final deconvolution kernel being a mean of maximum-normalized kernels across recordings divided by the sum of squared weights across time. The deconvolution kernel was biphasic and roughly similar to a derivative filter (that is, [-1,1]) (Extended Data Fig. 4b), consistent with rises in the GCaMP signal correspond to periods of spiking.

Retinotopic mapping

Cortical visual areas were mapped using visual sparse noise stimuli, which also provided the ‘passive context’ in our analyses. White squares 7.5° in length were presented asynchronously on a black background, with each square lasting 166 ms and about 12% of squares being present at any given time. Activity for each square presentation was averaged within a 300–500-ms time window (corresponding to the maximum GCaMP6s signal), and the average response to each square was bootstrapped 10 times. Visual field sign maps (Extended Data Fig. 2b) were calculated for each bootstrapped mean and then averaged. Visual field sign was defined by Gaussian-smoothing average square responses, finding the centre-of-mass for each cortical pixel relative to the square azimuth and elevation locations, determining the gradient within these azimuth and elevation centre-of-mass maps, and taking the sine of the difference between the azimuth and elevation gradients.

Neuropixels recordings

Electrophysiological recordings were made with Neuropixels Phase 3A probes³¹ affixed to metal rods and moved with micromanipulators (Sensapex). Raw data within the action potential band (soft high-pass filtered over 300 Hz) was denoised by common mode rejection (that is, subtracting the median across all channels), and spike-sorted using Kilosort 2 (www.github.com/MouseLand/Kilosort2). Units representing noise were manually removed using Phy⁵⁴. Multiunit activity was then defined as spikes pooled from all Kilosort-identified units within a given segment of the probe.

Electrophysiological recordings were synchronized to wide-field data and task events by aligning to a common digital signal randomly flipping between high and low states (produced from an Arduino) accounting for both clock offset and drift.

Light from the LED used during wide-field imaging produced a substantial artefact in the electrophysiological data. This artefact was reduced by ramping the light over 1 ms, and was removed from the action potential band by subtracting the average signal across all channels. Kilosort occasionally identified units from a small remaining artefact, which were readily identifiable from their shape and regularity and were discarded. The light artefact was removed from the LFP band (used in Extended Data Fig. 4c) by subtracting a rolling median light-triggered average for each LED colour.

Probe trajectories were reconstructed from histology (Extended Data Fig. 3a) using publicly available custom code (http://github.com/petersaj/AP_histology). Probe trajectories were estimated from wide-field images (Extended Data Fig. 3b) by manually identifying the probe in the image and transforming the location into CCF coordinates using the retinotopy–CCF alignment for that recording.

Striatal electrophysiology and depth-alignment

For striatal recordings, probes were inserted at approximately 200 μm anterior and 1,000 μm lateral to bregma at a 45° angle from horizontal (diagonally downwards) and 90° from the anterior–posterior axis (straight coronally) to a depth of about 6 mm along the probe axis to reach the contralateral striatum. Electrophysiological data were recorded with Open Ephys⁵⁵.

The borders of the striatum were identified within each recording using the ventricle and dorsolaterally neighbouring structure (endopiriform nucleus or claustrum) as electrophysiological landmarks. As no units were detected in the ventricle, the start of the striatum on the probe was marked as the first unit after at least a 200-μm gap from the last unit (or the top of the probe if no cortical units were detected). Detected units were continuous after the ventricle, but multiunit correlation in temporal bins of 10 ms and sliding spatial bins of 100 μm revealed a sharp border in correlation at a location consistent with the end of the striatum (Extended Data Fig. 3d). This lateral border of the striatum was present in every recording and used to define the end of the striatum on the probe.

Striatal recordings were aligned by depth using the lateral striatal border, as the lateral border was sharp; the medial border was inferred from lack of units and was therefore imprecise. The location of striatal units was then defined as distance from the lateral border, and depth-aligned analyses were performed on these distances divided into approximately 200-μm segments (Figs. 1f, 2a, b). Only depths present in >50% of recordings are shown, eliminating a sparse subset of medial depths in recordings with an unusually large portion of the probe corresponding to the striatum. Aligning by depth is only approximate, whereas aligning by functionally associated cortical maps provides a much more precise method of alignment (as discussed in ‘Striatal domain assignments’).

Single-unit analysis and striatal cell-type classification

High-quality single units were defined by the following criteria: (1) waveform trough to peak amplitude of more than 77 μV (based on a distribution of amplitudes); (2) minimum of 300 spikes; (3) less than 30% of spikes missing, estimated by fitting a Gaussian to the spike amplitude distribution with an additional cut-off parameter below which no spikes are present (using the Python function `scipy.optimize.curve_fit`); (4) waveform trough that preceded a waveform peak, to eliminate axonal spikes⁵⁶; (5) an estimated false-positive rate of less than 10% using a previously published approach⁵⁷. This estimates the false-positive rate F_p as the solution to $r = 2(\tau_r - \tau_c)n^2(1 - F_p)F_p/t$, in which r is the number of refractory period violations; τ_r is the refractory period (taken as 2 ms); τ_c is the censored period (taken as 0.5 ms), n is the number of spikes; and t is the total recording time. The built-in function ‘roots’ of MATLAB was used for this. If an imaginary number was returned by the function, owing to r being too high, the F_p rate was set to 1 as previously published⁵⁷, and the unit rejected.

Units passing these quality criteria were then classified into four putative striatal cell types: MSNs, FSIs, TANs and a fourth class of unidentified interneurons (Extended Data Fig. 10). Neurons with narrow waveforms (Kilosort template trough-to-peak waveform duration ≤ 400 μs) were identified as either FSIs or unidentified interneurons, as previously published³⁷. Putative FSIs and unidentified interneurons were then separated using the proportion of time associated with long interspike-intervals (>2 s) by summing inter-spike intervals longer than 2 s and dividing the sum by the total recording time

Article

(as calculated in previously published³⁸): neurons for which this ratio was more than 10% were classified as unidentified interneurons and the others as FSIs. The remaining units were presumed to be TANs and MSNs, which were further separated using the post-spike suppression. We measured the length of time that the firing rate of a unit was suppressed following an action potential by counting the number of 1-ms bins in its autocorrelation function until the firing rate of the unit was equal or greater to its average firing rate over the 600-ms to 900-ms autocorrelation bins. Units with post-spike suppression of >40 ms were labelled TANs, and the remaining units were labelled MSNs. A few units had short waveforms (<400 μ s) and long post-spike suppression (>40 ms). These units were very rare (36 out of 8,303) and exhibited TAN-like responses and might therefore be TAN neurites; they were excluded from further analysis.

Cortical electrophysiology and alignment

For cortical recordings, a second craniotomy was performed over VISam targeted by retinotopic visual-field sign maps relative to vasculature. During recording, a second Neuropixels probe was inserted into VISam at a 45° angle from horizontal (diagonally downwards) and 90° from the anterior–posterior axis (straight coronally) to a depth of about 2 mm along the probe axis.

Cortical depth was aligned across recordings using current source density analysis. Mice were passively presented with visual gratings, and the current source density was computed as the second spatial derivative of the stimulus-triggered average local field potential signal, smoothed by a boxcar rolling average of 10 channels. The average current source density 40–60 ms after the stimulus was then aligned across recordings by interpolation using the maximum sink (Extended Data Fig. 4c, red patch) and the first source (Extended Data Fig. 4c, top blue patch). The ‘aligned visual cortex depth’ (Extended Data Fig. 4c) was then set relative to these points, with the first source being 0 and the maximum sink being set to the median source-sink distance across sessions. Superficial and deep layers were defined as being above or below midway from the sink to the lower source (Extended Data Fig. 4c, horizontal line). The ventral border of the cortex was made clear by a gap in detected units corresponding to the white matter.

Regression from task events to activity

Regression from task events to striatal multiunit activity or deconvolved cortical fluorescence was performed using linear regression of the form

$$\begin{pmatrix} F_{t1} \\ \vdots \\ F_{tn} \end{pmatrix} \sim \begin{pmatrix} \text{Event}_{1,\text{lag } 1,t1} & \cdots & \text{Event}_{n,\text{lag } n,t1} \\ \vdots & \ddots & \vdots \\ \text{Event}_{1,\text{lag } 1,tn} & \cdots & \text{Event}_{n,\text{lag } n,tn} \end{pmatrix} * K_{\text{task} \rightarrow \text{activity}}$$

Here, $K_{\text{task} \rightarrow \text{activity}}$ represents a vector containing the concatenated estimated kernels for each event type, estimated by least squares using the \ operator of MATLAB. F_{t1} to F_{tn} represent the fluorescence or firing rate time course to be predicted, ‘baseline-subtracted’ by subtracting the average combined activity –0.5–0 s before all stimulus onsets, during which times the mice were required not to turn the wheel. For each event type, a task matrix was constructed as a sparse Toeplitz matrix with a diagonal series of 1s for each event at each time lag, with zeros elsewhere. Toeplitz matrices were made for each event type: stimulus onset (one for each stimulus side * contrast, lags of 0–0.5 s), movement onset (one each for left and right final response, lags of –0.5–1 s), ‘go’ cue onset (one for trials in which mice had already begun moving and one for trials with no movement before the cue, lags of 0–0.5 s), and outcome (one for water and one for white noise, lags of 0–0.5 s). These matrices were horizontally concatenated to produce the matrix shown in the above equation. Regression was fivefold cross-validated by splitting up time points into consecutive chunks.

Regression from cortical activity to striatal activity

Normalized, haemodynamically corrected and deconvolved wide-field fluorescence was regressed to striatal multiunit activity using ridge regression. Regression took the form

$$\begin{pmatrix} F_{t1} \\ \vdots \\ F_{tn} \\ 0 \\ \vdots \\ 0 \\ 0 \end{pmatrix} \sim \begin{pmatrix} \text{SV}_{1,\text{lag } 1,t1} & \cdots & \text{SV}_{n,\text{lag } n,t1} & 1 \\ \vdots & \ddots & \vdots & \vdots \\ \text{SV}_{1,\text{lag } 1,tn} & \cdots & \text{SV}_{n,\text{lag } n,tn} & 1 \\ \lambda & 0 & 0 & 0 \\ \vdots & \vdots & \vdots & \vdots \\ 0 & 0 & \lambda & \vdots \\ 0 & 0 & 0 & 0 \end{pmatrix} * K_{\text{cortex} \rightarrow \text{striatum}}$$

Here F_{t1} to F_{tn} represent the standard-deviation-normalized striatal spiking time course to be predicted. $K_{\text{cortex} \rightarrow \text{striatum}}$ represents the estimated spatiotemporal kernel from cortical fluorescence to standard-deviation-normalized striatal spiking estimated by least squares using the \ operator of MATLAB. To make the design matrix, a Toeplitz matrix was constructed for each temporal SVD component of the cortical wide-field, scaled by the singular values (S*V), staggered across a range of time values (–100 ms to 100 ms). These Toeplitz matrices were horizontally concatenated, also including a column of ones to allow an offset term. To regularize using ridge regression, this matrix was vertically concatenated above diagonal matrix of regularization values λ , and the striatal activity time courses F were concatenated above the same number of zeros. Regression was fivefold cross-validated by splitting up time points into consecutive chunks, and values for λ were determined empirically for each experiment by regressing from cortical fluorescence to multiunit from the whole striatum across a range of λ values and finding the λ that yielded the largest cross-validated explained variance.

Striatal domain assignments

Striatal domains were defined from cortical maps as spatial kernels (time lag = 0) described in ‘Regression from cortical activity to striatal activity’ for consecutive 200- μ m segments of the Neuropixels track through the striatum recorded in each experiment. The cortical maps were combined across all sessions and mice, and split into three groups through K -means, and the average cortical map for each group was used as a template for each striatal domain. The spatial map from each 200- μ m striatal segment was then assigned to one group by highest correlation with the template maps. Striatal domain assignments were smoothed using a three-segment median filter and restricted to a standard order by replacing misordered assignments with their nearest neighbour. This process ensured contiguous domains and was empirically successful at removing rare aberrations. Our DMS, DCS and DLS approximately correspond to the medial dorsomedial subdivision, lateral dorsomedial subdivision, and dorsolateral domains of a previous publication² and the domains i.dm.d/dm/im, i.dm.cd/i.vl.cvl, and i.vl.v/vt in ref.¹.

Multiunit activity for each domain and session was created by pooling all spikes within striatal segments assigned to a given domain. Multiunit activity was expressed as $\Delta\text{FR}/\text{FR}_0$, being the firing rate baseline-subtracted (average from 0.5–0 s before stimulus onset in each trial) and divided by the average firing rate across all baseline time points plus a 10 spikes per second softening factor.

Cortical regions of interest for striatal domains

Cortical regions of interest corresponding to the most correlated cortical region for each striatal domain (used in Figs. 4c–d, 5a, Extended Data Fig. 9d) were generated using the template cortical map for each domain described in ‘Striatal domain assignments’. Pixels were thresholded above 75% of the maximum weighted pixel and contralateral pixels and clusters smaller than 100 pixels were removed, resulting in a discrete cortical region of interest over the region most correlated with each striatal domain.

Allen connectivity maps

Anatomical projections were labelled using the Allen Mouse Brain Connectivity Atlas¹⁸ (Fig. 2h) (© 2015 Allen Institute for Brain Science. Allen Brain Atlas API. Available from brain-map.org/api/index.html). The API was queried for injection sites within the cortex that yielded axon terminals in each striatal domain, and the seed points used for each striatal domain were the centre-of-mass for each domain relative to the longest recorded striatal length and interpolated into the targeted striatal trajectory in the CCF atlas (shown in Fig. 2e). To maximize coverage across the brain (as the Allen Mouse Brain Connectivity Atlas has different left and right hemisphere injections), queries were performed for striatal sites bilaterally and results from the right striatum were mirrored and combined with the results from the left striatum. The cortical sites with striatal projections returned by the API were then plotted as a heat map by binning across space and blurring with a Gaussian filter.

Muscimol experiments

For inactivation experiments, in the same surgery that placed a craniotomy with access to the striatum, a second craniotomy was performed over VISam targeted by retinotopic visual field sign maps relative to vasculature. During the experiment, mice performed the task for approximately half of the normal number of trials and were then shown visual noise stimuli and passive gratings. Muscimol (Sigma, 5 mM in ACSF) was then applied topically by placing muscimol-soaked gelfoam in VISam craniotomy for 40 min, with additional ACSF applied at 20 min to prevent drying. Mice then performed the task until they no longer engaged and were again shown visual noise stimuli and passive gratings.

The effect of topical muscimol by cortical depth was assessed in two separate mice (Extended Data Fig. 9a) by inserting a Neuropixels probe near the edge of a craniotomy and recording activity before and after muscimol application.

In sessions with cortical inactivation, mice performed the task as described in 'Visually guided wheel-turning task' without the inclusion of repeat trials for incorrect 50% and 100% contrast stimuli. This was normally included to discourage bias and was excluded in these sessions to allow for a muscimol-induced bias.

Reporting summary

Further information on research design is available in the Nature Research Reporting Summary linked to this paper.

Data availability

The datasets generated during the current study are available as downloadable files at <https://osf.io/x4q26/>.

Code availability

The code used to analyse the data are available at https://github.com/petersaj/Peters_et_al_Nature_2021.

- Steinmetz, N. A. et al. Aberrant cortical activity in multiple GCaMP6-expressing transgenic mouse lines. *eNeuro* **4**, ENEURO.0207-17.2017 (2017).
- Bhagat, J., Wells, M. J., Harris, K. D., Carandini, M. & Burgess, C. P. Rigbox: An open-source toolbox for probing neurons and behavior. *eNeuro* **7**, ENEURO.0406-19.2020 (2020).
- Wang, Q. et al. The Allen mouse brain common coordinate framework: a 3D reference atlas. *Cell* **181**, 936–953.e20 (2020).
- Zhuang, J. et al. An extended retinotopic map of mouse cortex. *eLife* **6**, e18372 (2017).
- Rossant, C. et al. Spike sorting for large, dense electrode arrays. *Nat. Neurosci.* **19**, 634–641 (2016).
- Siegle, J. H. et al. Open Ephys: an open-source, plugin-based platform for multichannel electrophysiology. *J. Neural Eng.* **14**, 045003 (2017).
- Deligkaris, K., Bullmann, T. & Frey, U. Extracellularly recorded somatic and neuritic signal shapes and classification algorithms for high-density microelectrode array electrophysiology. *Front. Neurosci.* **10**, 421 (2016).
- Hill, D. N., Mehta, S. B. & Kleinfeld, D. Quality metrics to accompany spike sorting of extracellular signals. *J. Neurosci.* **31**, 8699–8705 (2011).

Acknowledgements We thank C. Reddy, M. Wells, L. Funnell and H. Forrest for mouse husbandry and training; R. Raghupathy, I. Pranker and D. Orme for histology; D. Cohen for helpful discussions; and NVIDIA for donation of a Titan X GPU. This work was supported by a Newton International Fellowship, EMBO Fellowship (ALTF 1428-2015), and a Human Frontier Science Program Fellowship (LT226/2016-L) to A.J.P., a Wellcome Trust PhD Studentship to J.M.J.F., a Human Frontier Science Program Fellowship (LT001071/2015-L) and Marie Skłodowska-Curie fellowship of the EU Horizon 2020 (656528) to N.A.S., Wellcome Trust grants 205093, 204915 to K.D.H. and M.C. and ERC grant 694401 to K.D.H. M.C. holds the GlaxoSmithKline/Fight for Sight Chair in Visual Neuroscience.

Author contributions A.J.P., K.D.H. and M.C. conceived and designed the study. A.J.P. collected and analysed data. J.M.J.F. analysed cell types and single-unit data. N.A.S. developed wide-field imaging and Neuropixels setups. A.J.P., K.D.H. and M.C. wrote the manuscript with input from J.M.J.F. and N.A.S.

Competing interests The authors declare no competing interests.

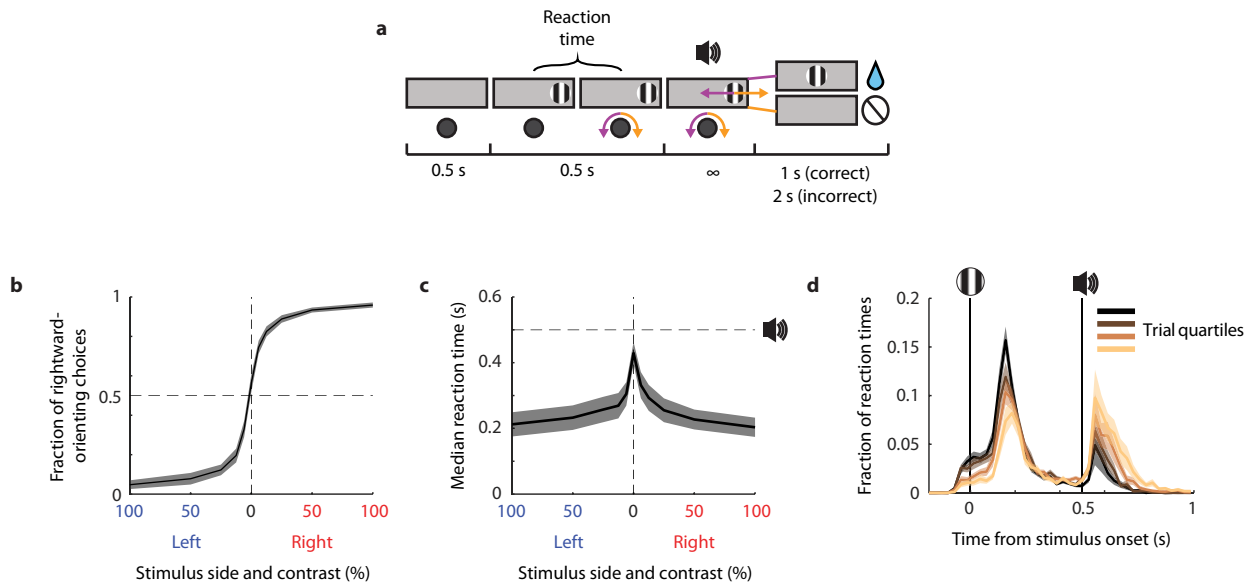
Additional information

Supplementary information The online version contains supplementary material available at <https://doi.org/10.1038/s41586-020-03166-8>.

Correspondence and requests for materials should be addressed to A.J.P.

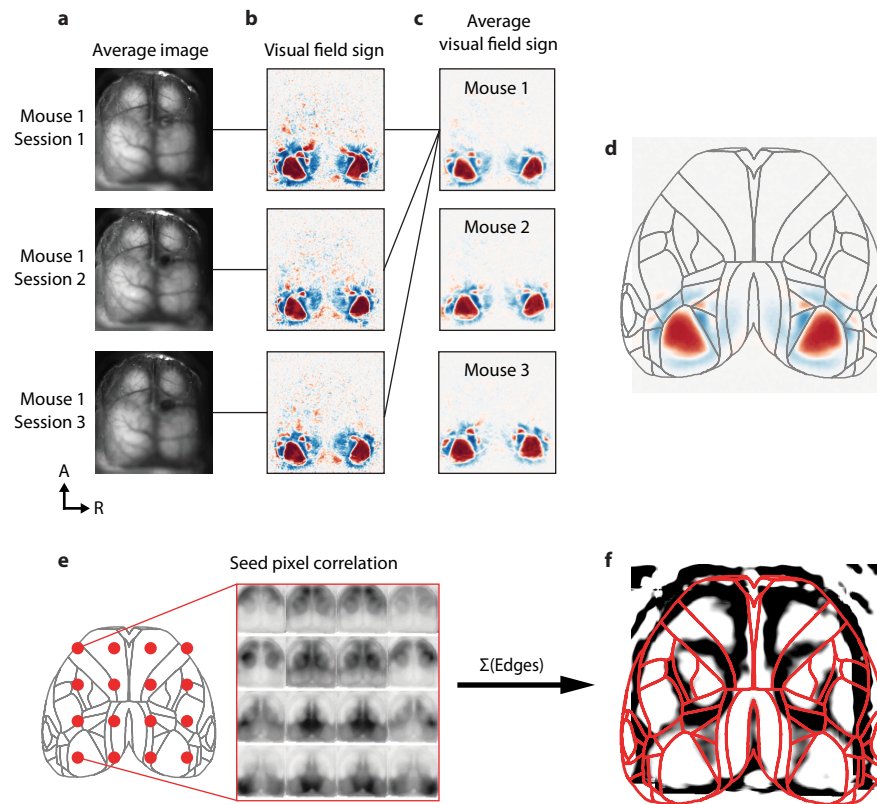
Peer review information Nature thanks the anonymous reviewer(s) for their contribution to the peer review of this work.

Reprints and permissions information is available at <http://www.nature.com/reprints>.



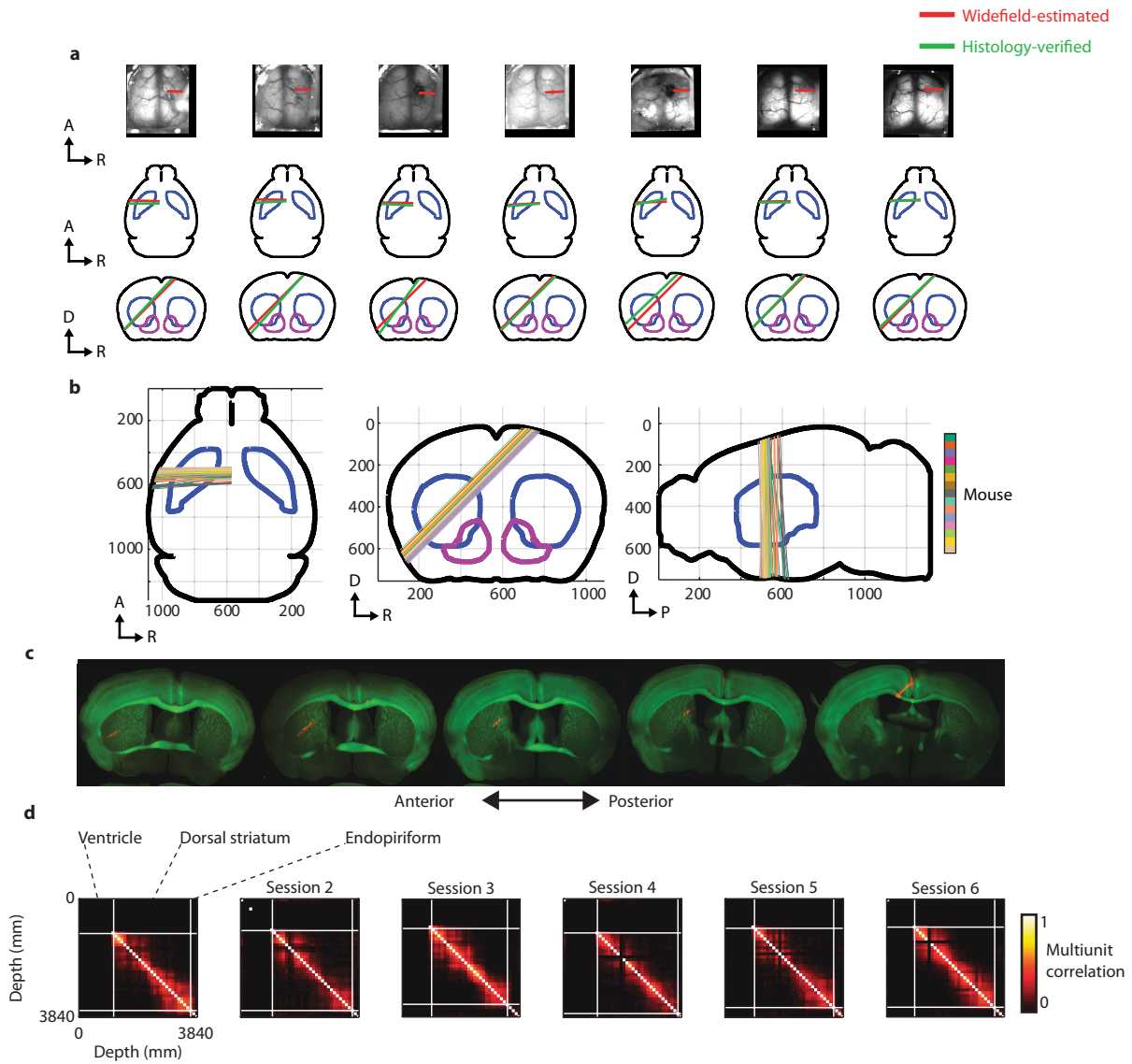
Extended Data Fig. 1 | Task performance. a, Timeline of events in a trial. After 0.5 s with no wheel movement, a stimulus appears. The mouse may turn the wheel immediately, but it only becomes yoked to the stimulus after a further 0.5 s, at which time an auditory 'go' cue is played. If the mouse drives the stimulus into the centre, a water reward is delivered and a new trial begins after 1 s; if the mouse drives the stimulus off the screen away from the centre, a white noise sound is played and a new trial begins after 2 s. **b,** Psychometric curve showing task performance: the fraction of choices as a function of stimulus

contrast and side. Curve and shaded region show mean \pm s.e. across sessions. **c,** Median reaction time as a function of stimulus contrast and side as in **b** (mean \pm s.e. across each session's median). Dotted horizontal line indicates time of auditory 'go' cue. **d,** Histogram of times from stimulus to movement onset (reaction time) by trial quartile within sessions (first quarter of trials in the session in black, last quarter in beige; mean \pm s.e. across mice). In early trials, mice typically begin moving the wheel before the cue. Later in the sessions, they waited more often for the cue.



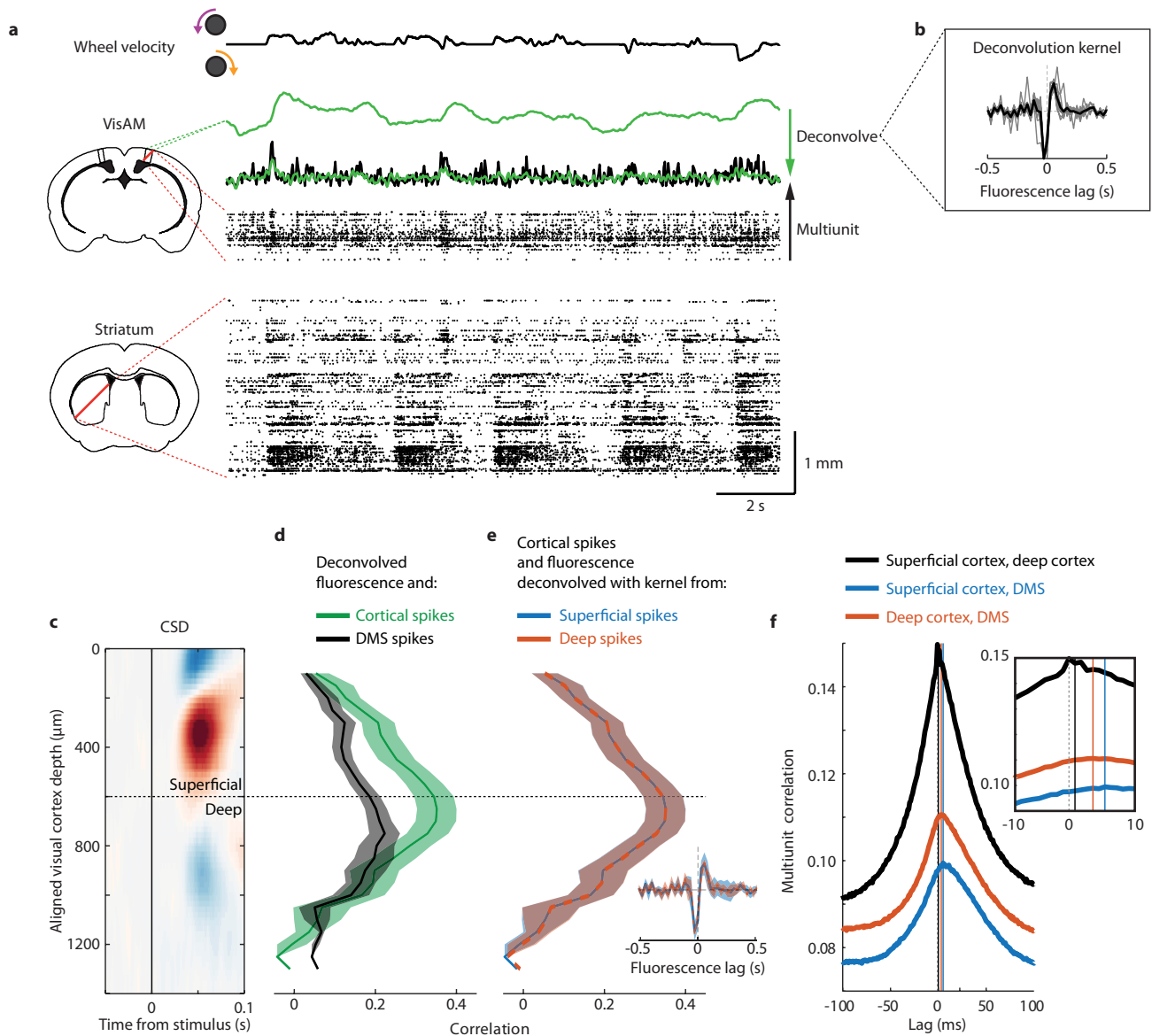
Extended Data Fig. 2 | Cortical wide-field alignment. **a**, Example wide-field images from one mouse, used to align vasculature. **b**, Retinotopic visual field sign maps corresponding to the sessions in **a**. **c**, Retinotopic maps averaged across all sessions for three example mice, used to align wide-field images across mice. **d**, Retinotopic map averaged across mice and symmetrized, used to align wide-field images to the Allen CCF atlas (used only for figure overlay purposes). **e**, Cortical seed pixels (left) and corresponding pixel–pixel correlation maps (right). Each pixel–pixel correlation map (right) is made by correlating a given pixel with all other pixels, which reveals clusters of pixels belonging to correlated cortical regions (for example, the central circles corresponding to limb somatomotor cortex). **f**, Summed edge-filtered

pixel–pixel correlation maps (as in **e**) showing the outlines of correlated clusters of pixels. Each pixel–pixel correlation map (as in **e**) highlights a correlated cluster of pixels. Edge-filtering each pixel–pixel correlation map then draws a boundary around the highlighted correlated cluster. Summing these edges across all pixel–pixel correlation maps illustrates the boundaries of all correlated clusters of pixels, prominently including limb somatomotor cortex (central circles), visual cortex (posterior lateral triangular regions), retrosplenial cortex (posterior medial region) and orofacial somatomotor cortex (frontal lateral regions). The Allen CCF regions aligned using retinotopy (red) align well to correlation borders, indicating that our alignment methods based on posterior retinotopy also successfully align anterior regions.



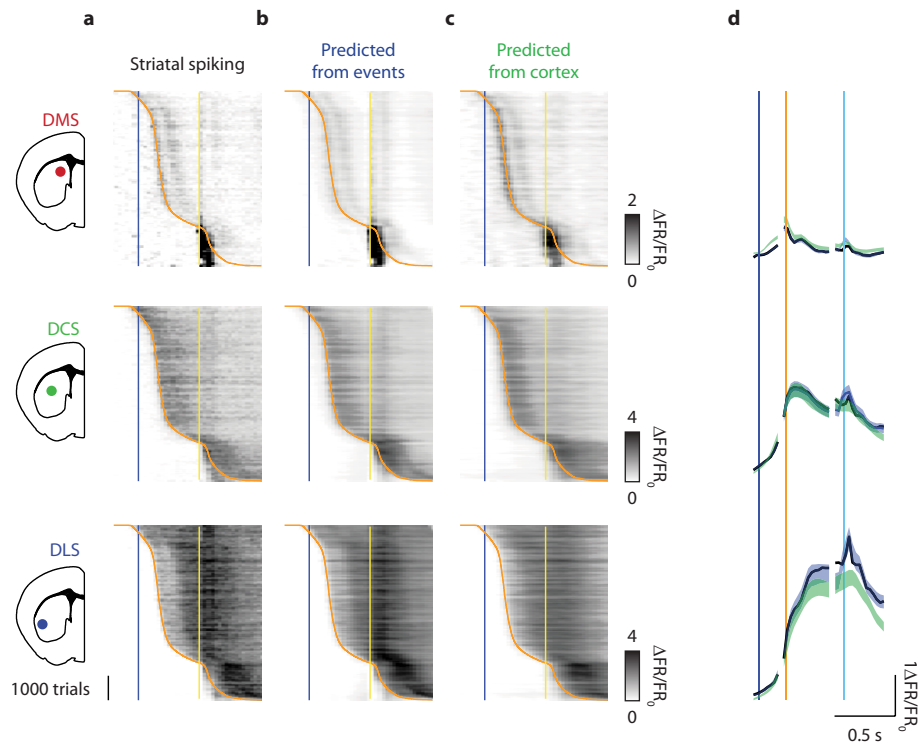
Extended Data Fig. 3 | Striatal recording locations and electrophysiological borders. **a**, Top, wide-field images used to approximate probe location (red line); middle and bottom, horizontal and coronal views of the brain with wide-field-estimated probe location (red line) and histologically verified probe location (green line). Black outline, brain; blue outline, dorsal striatum; purple outline, ventral striatum. Wide-field-estimated probe locations closely match histologically verified probe locations.

b, Wide-field-estimated probe location of all trained mice plotted in Allen CCF coordinates. **c**, Example histology showing GCaMP6s fluorescence (green) and dye from the probe (red). **d**, Example multiunit correlation matrix by location along the probe for several sessions in the mouse from **c**, with the borders of the striatum approximated medially by the lack of spikes in the ventricle and laterally by the sudden drop in local multiunit correlation. Dye from **c** corresponds to session 1 in **d** and histology-validated regions are labelled.



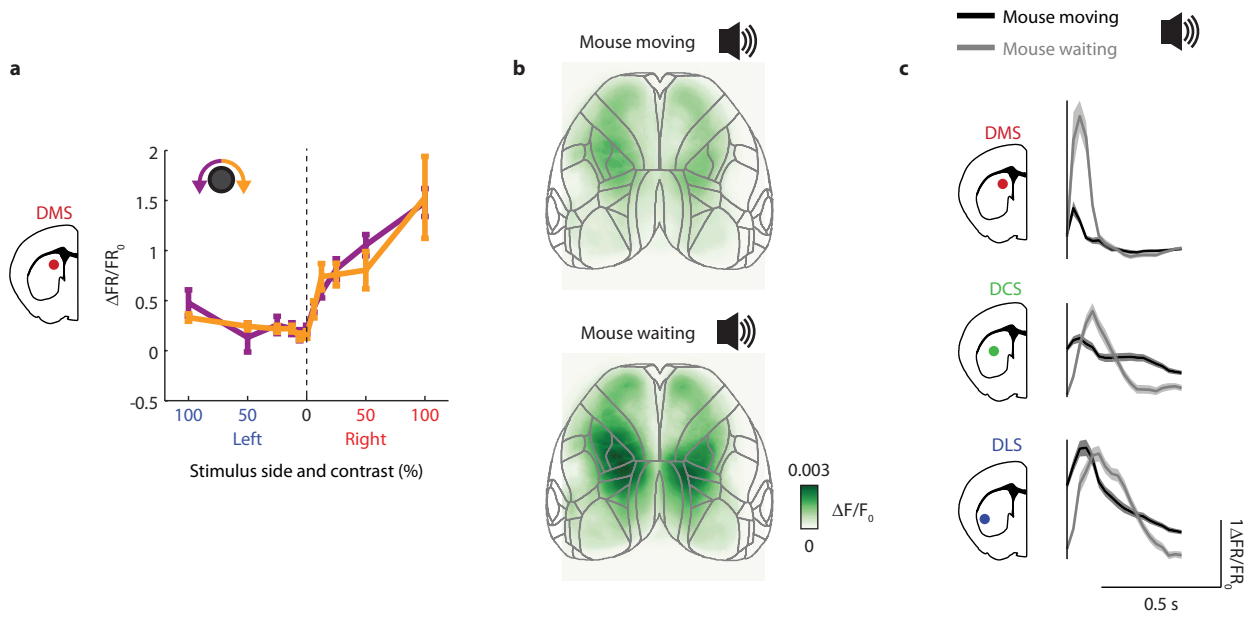
Extended Data Fig. 4 | Relationship of cortical spiking with cortical fluorescence and with striatal spiking. a, Example triple recording with wide-field imaging, VISam electrophysiology and striatal electrophysiology during the task. **b**, Deconvolution kernel obtained by predicting cortical multiunit spikes from cortical fluorescence around the probe (black, mean; grey, individual sessions). **c**, Current source density (CSD) from average stimulus responses aligned and averaged across sessions, used to identify superficial and deep cortical layers. Horizontal dashed line represents the estimated border between superficial and deep layers. **d**, Correlation of VISam spiking with deconvolved fluorescence (green) and DMS spiking (black) (mean \pm s.e. across sessions). Cortical fluorescence and striatal spiking are both correlated to cortical spiking along a similar depth profile (correlation between fluorescence and striatal depth profiles compared to depth-shifted

distribution, $r = 0.57 \pm 0.14$ (mean \pm s.e.) across 10 sessions, $P = 9.0 \times 10^{-4}$). **e**, Correlation of VISam spiking with fluorescence deconvolved with a kernel created only using superficial spikes (blue) or deep spikes (orange) (mean \pm s.e. across sessions). Inset, deconvolution kernels as in **b** created using only superficial or deep spikes. Kernels created from superficial or deep spikes are not different (two-way ANOVA on time and depth, depth $P = 1$ across 10 sessions) and correlation between spikes and deconvolved fluorescence does not depend on kernel (two-way ANOVA on depth and kernel, kernel $P = 0.97$), indicating the deconvolution kernel is related to GcaMP6s dynamics consistently across depths. **f**, Cross-correlation of multiunit activity across superficial cortex, deep cortex and DMS. Inset, zoomed-in plot. Deep cortical spiking leads striatal spiking by about 3 ms (orange vertical line).



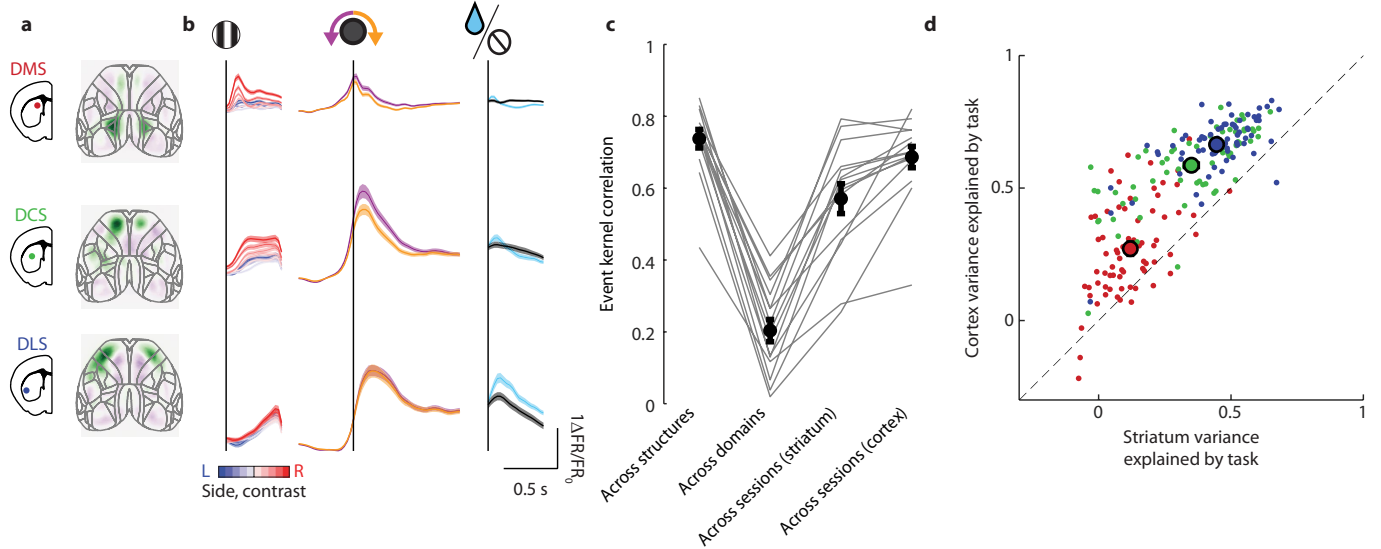
Extended Data Fig. 5 | Striatal activity during trials with ipsilateral stimuli and ipsilaterally orienting movements. **a**, Activity for each striatal domain across all trials from all sessions with ipsilateral stimuli, ipsilaterally orienting movements and rewards, formatted as in Fig. 3a. Trials are sorted vertically by reaction time. Blue line, stimulus onset; orange curve, movement onset; yellow line, 'go' cue. Activity within each time point is smoothed with a running average of 100 trials to display across-trial trends. **b**, Prediction of activity in

each striatal domain by summing kernels for task events, formatted as in Fig. 3c. **c**, Prediction of striatal activity from cortical activity, formatted as in Fig. 3d. **d**, Trial-averaged activity in each striatal domain (black), predicted from task events (blue), and predicted from cortical activity (green), aligned to stimulus (blue line), movement (orange line) and reward (cyan line) (mean \pm s.e. across sessions), formatted as in Fig. 3e.



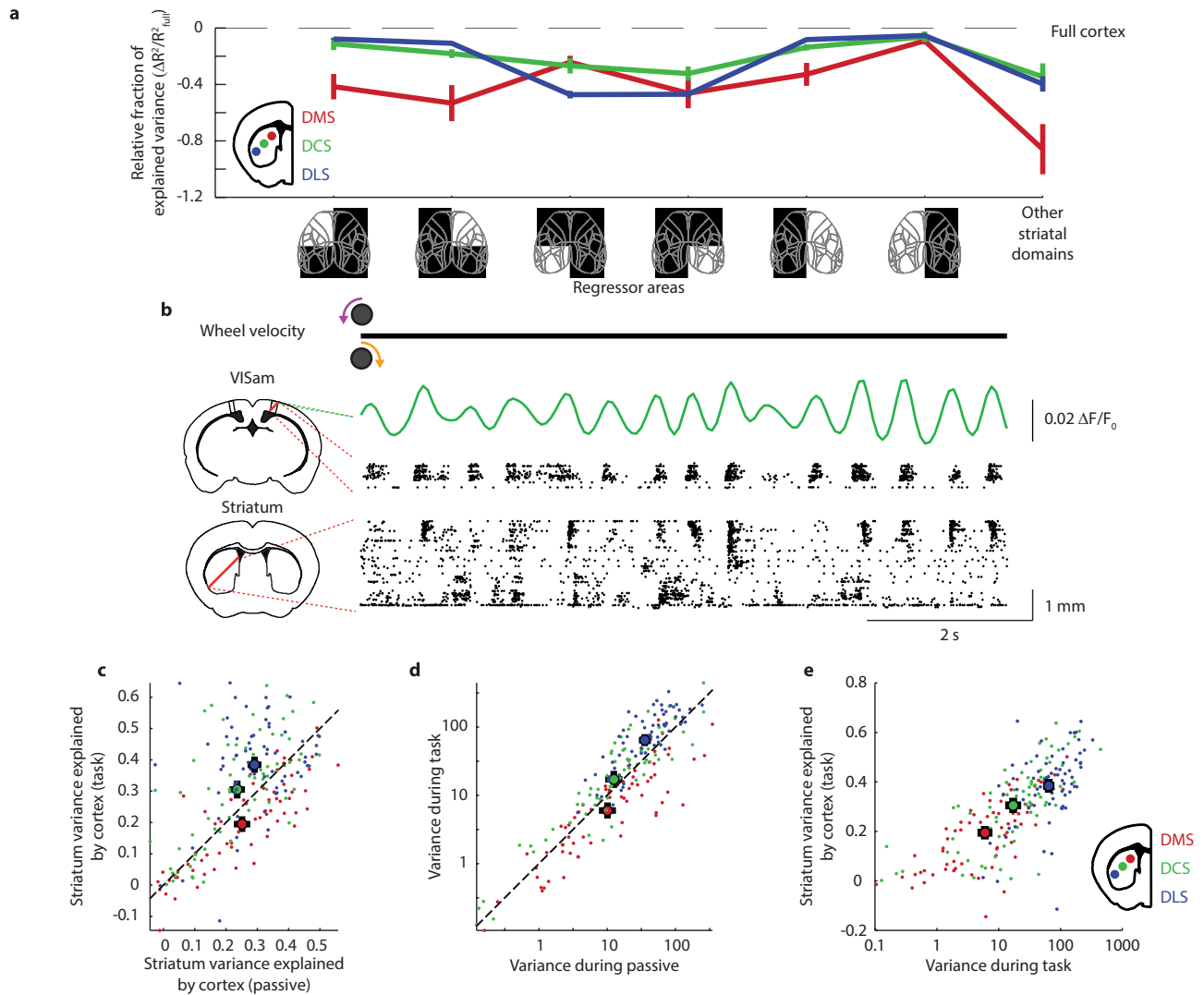
Extended Data Fig. 6 | Visual responses in dorsomedial striatum do not depend on upcoming movement choice and responses to the auditory ‘go’ cue are suppressed by ongoing movement. a. Curves show average stimulus response (0–0.2 s after stimulus onset) in DMS, as a function of contrast and side, for trials with <500-ms reaction times and contralateral-orienting (purple) or ipsilateral-orienting (orange) movements (mean \pm s.e. across sessions). Movement choice does not affect stimulus responses, indicating that stimulus responses are purely sensory, rather than linked to decisions

(two-way ANOVA on stimulus and choice, interaction $P=0.56$ for 77 sessions). **b.** ‘Go’ cue kernel (lag = 50 ms after cue shown) obtained when fitting cortical activity from task events, for trials with movement onset before the cue (top) and after the cue (bottom). **c.** ‘Go’ cue kernel obtained when fitting activity in each striatal domain from task events as in Fig. 3b, for trials with movement onset before the cue (black) and after the cue (grey). In both parietal cortex and DMS, responses to the ‘go’ cue are much larger when the mouse is not moving.



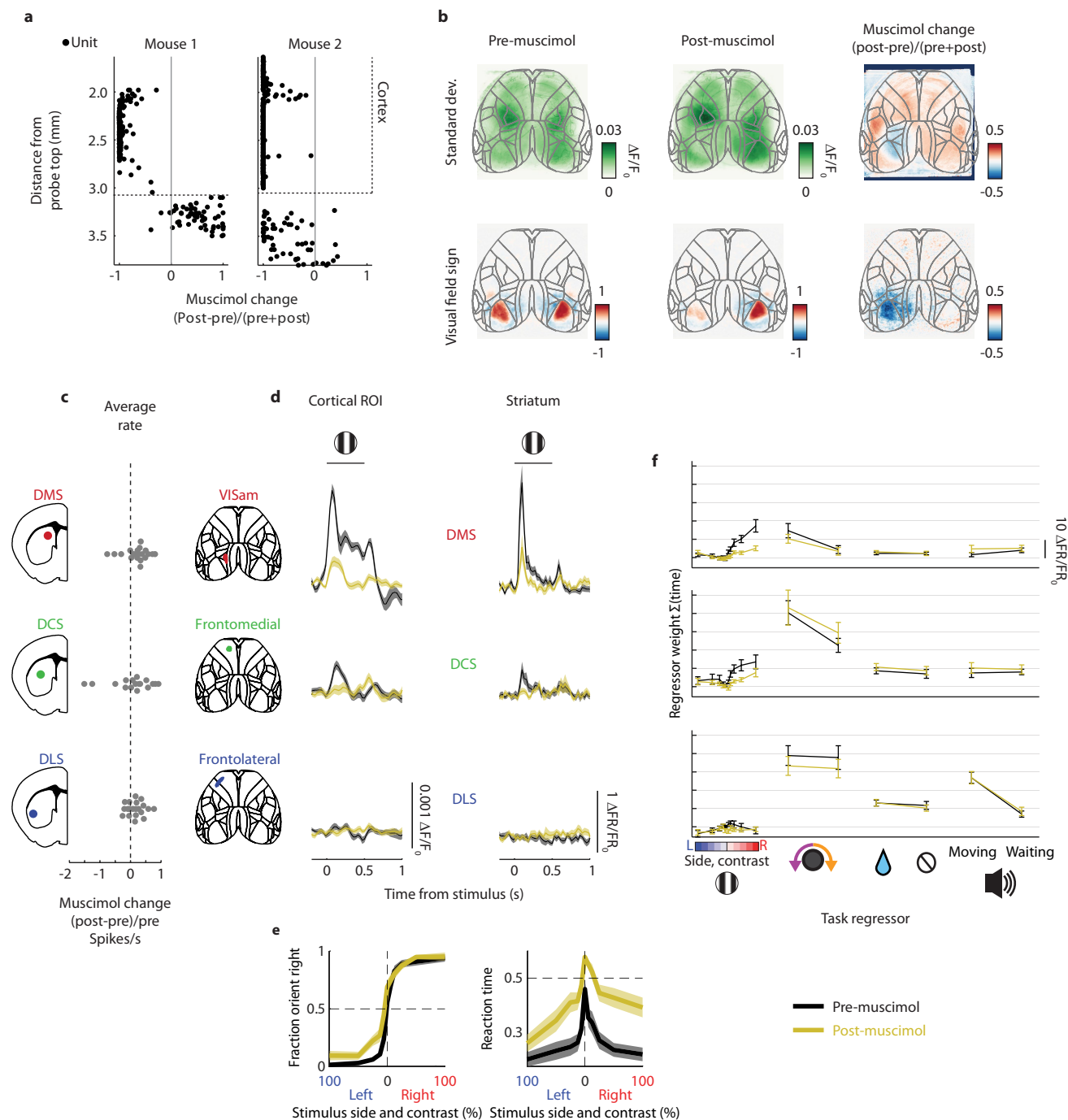
Extended Data Fig. 7 | Task kernels for cortical activity associated with each striatal domain match task kernels for striatal activity. **a**, Cortical maps used to define cortical activity associated with each striatal domain (from Fig. 2f, producing activity in Fig. 3d). **b**, Temporal kernels obtained when fitting cortical activity from task events for stimuli (left), movements (middle), and outcome (right) (mean \pm s.e. across sessions), formatted as in Fig. 3b. **c**, Correlation of task kernels for striatal and cortical activity. Columns from left to right: correlation of associated striatal and cortical kernels, within the same session; correlation of striatal kernels for different domains within the same session; correlation of striatal kernels from different sessions but the same striatal domain, and correlation of cortical kernels obtained from different sessions, but associated with the same striatal domain. Grey lines show single sessions; black points and error bars show mean \pm s.e. across mice.

The kernels obtained for associated striatal domains and cortical regions are more correlated than kernels for different striatal domains (signed-rank test, $P = 6.1 \times 10^{-5}$ for 15 mice), indicating task kernels are domain-specific and shared between associated cortical and striatal regions. Correlations are also higher between associated striatal and cortical activity within-sessions, than between kernels fit to the same striatal domain on different sessions (signed-rank test, $P = 1.2 \times 10^{-4}$), indicating that differences between cortical and striatal task responses are smaller than session-to-session variability. **d**, Cross-validated fraction of variance explained by task events for striatal activity versus associated cortical activity. Small dots, sessions; large dots, mean \pm s.e. across sessions; colour, striatal domain. Explained variance from task events is correlated between the cortex and striatum (correlation, $r = 0.68$, $P = 1.14 \times 10^{-10}$ across 77 sessions).



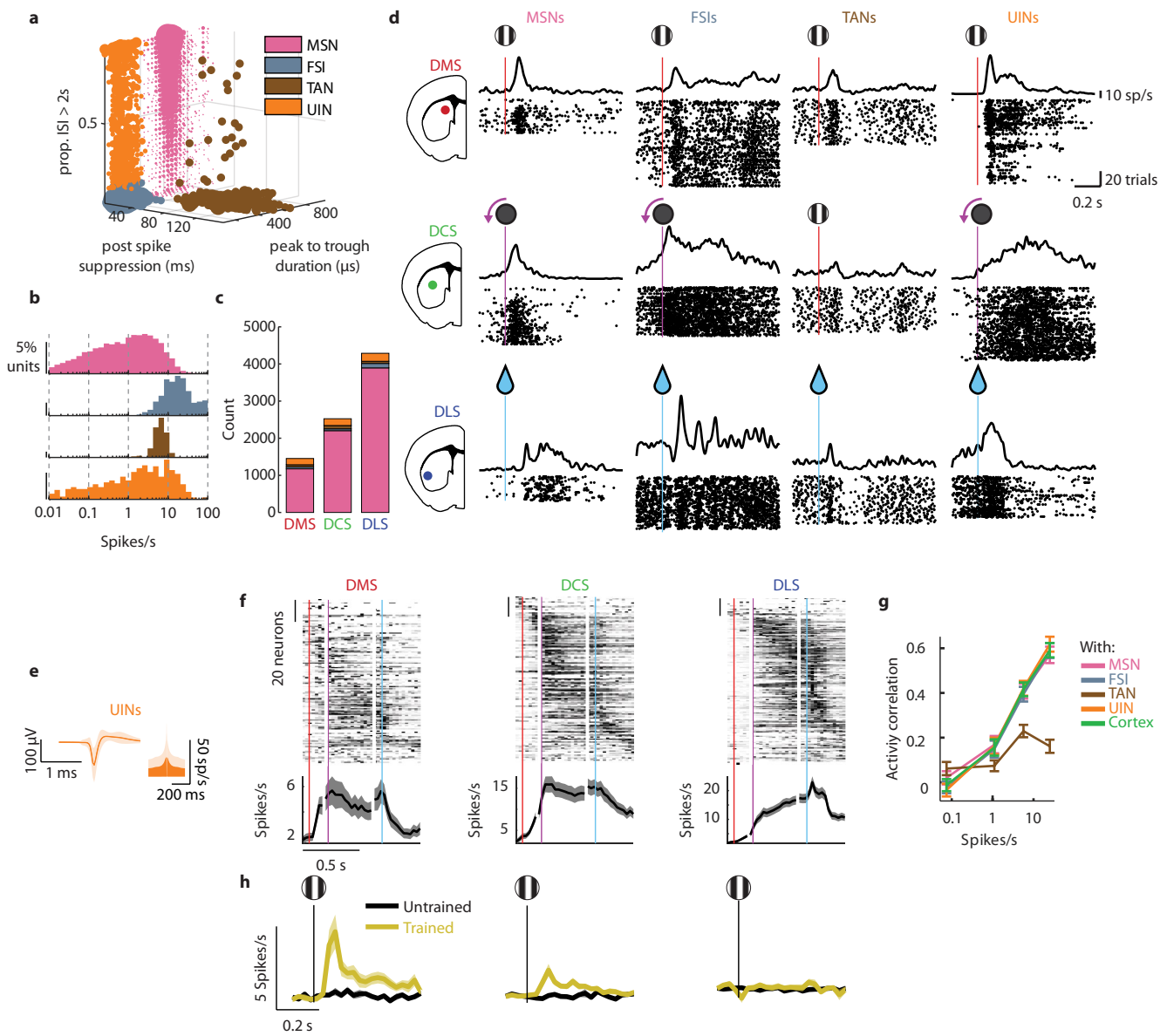
Extended Data Fig. 8 | Prediction of striatal activity from subregions of cortex, from other striatal domains, and from the cortex during passive periods. **a**, Activity in each striatal domain predicted from subregions of cortex (indicated by white regions in diagrams below *x*-axis) or from the other two striatal domains (far right). Each curve shows the relative cross-validated fraction of explained variance ($(R^2_{\text{region}} - R^2_{\text{full cortex}})/R^2_{\text{full cortex}}$) for the colour-coded striatal domain (mean \pm s.e. across sessions). Predictions are best from the associated cortical regions (two-way ANOVA on session and cortical subregion, subregion $DMS P = 4.6 \times 10^{-3}$, $DCS P = 4.8 \times 10^{-5}$, $DLS P = 3.1 \times 10^{-85}$ across 77 sessions) and striatal activity is less well predicted from other striatal domains than from cortex (signed-rank test, $DMS P = 1.6 \times 10^{-10}$, $DCS P = 2.1 \times 10^{-5}$, $DLS P = 8.4 \times 10^{-10}$ across 77 sessions). **b**, Example wheel trace, deconvolved cortical fluorescence, visual cortical electrophysiology and striatal electrophysiology session in the passive context (viewing visual noise stimuli), showing coherent low-frequency oscillations in VISam and DMS

(formatted as in Extended Data Fig. 4a, from the same session session). **c**, Cross-validated fraction of striatal variance explained from cortex in task versus passive contexts. Small dots, sessions; large dots, mean \pm s.e. across sessions; colour, striatal domain. DMS is predicted slightly better from cortex in the passive state, but DCS and DLS are predicted slightly worse the passive state (signed-rank test, $DMS P = 6.2 \times 10^{-7}$, $DCS P = 1.9 \times 10^{-4}$, $DLS P = 1.6 \times 10^{-5}$ across 77 sessions). **d**, Variance of striatal activity across task and passive states, legend as in **b**. During the passive state, DMS exhibits more variance and DCS and DLS exhibit less variance (signed-rank test, $DMS P = 3.0 \times 10^{-6}$, $DCS P = 1.3 \times 10^{-4}$, $DLS P = 1.1 \times 10^{-10}$ across 77 sessions), matching the differences in predictability between states. **e**, Cross-validated fraction of striatal explained variance from the cortex vs. variance of striatal activity during task performance, legend as in **b**. Cortex-explained variance is consistently related to activity variance across domains (ANCOVA, domain $P = 0.22$, domain-activity variance interaction $P = 0.76$).



Extended Data Fig. 9 | Visual cortical inactivation selectively eliminates striatal visual responses. **a**, Cortical unit firing rate change across topical muscimol application. Horizontal dotted line indicates bottom edge of cortex. Topical muscimol effectively silences the full cortical depth. **b**, Deconvolved cortical fluorescence standard deviation (top) and retinotopic visual field sign (bottom) before and after muscimol application. Muscimol was centred on VISam and spread laterally to other visual areas. **c**, Relative firing rate change in each striatal domain before and after cortical inactivation (dots are sessions). Firing rate increases slightly after cortical inactivation (signed-rank test, DMS $P=0.04$, DCS $P=0.02$, DLS $P=0.02$ across 22 sessions). **d**, Passive responses to visual stimuli in cortical regions of interest (left) and corresponding striatal domains (right) before (black) and after (yellow) inactivation of visual cortex. Muscimol reduced the stimulus response in VISam and DMS proportionally within each session (correlation between fractional reduction of each area:

$r=0.48$, $P=0.04$ across 22 sessions). **e**, Psychometric curve (left) and median reaction time (right) as a function of stimulus contrast and side as in Extended Data Fig. 1b, before (black) and after (yellow) muscimol in visual cortex (mean \pm s.e. across sessions). Task performance becomes worse asymmetrically across stimuli (two-way ANOVA on stimulus and condition, interaction $P=0.04$ across 22 sessions) and reaction times become longer across stimuli (two-way ANOVA on stimulus and condition, condition $P=1.1 \times 10^{-26}$ across 22 sessions). **f**, Kernels using task events to predict striatal activity before (black) and after (yellow) visual cortical muscimol (mean \pm s.e. across sessions). Stimulus kernel weights decrease after muscimol while other kernel weights do not change significantly (two-way ANOVA on regressor and condition, condition effect on stimuli regressors DMS $P=2.0 \times 10^{-7}$, DCS $P=8.4 \times 10^{-6}$, DLS $P=0.03$, $P>0.05$ for other domains and regressors across 22 sessions).



Extended Data Fig. 10 | Identifying striatal cell types with electrophysiology, and unidentified interneuron activity.

a, Electrophysiological properties used to classify striatal cell types. Striatal cells were identified as MSNs, FSIs, TANs and a fourth class of unidentified interneurons, according to waveform duration, length of post-spike suppression, and fraction of long interspike intervals. **b**, Histogram of firing rates across all units within each cell type. **c**, Number of units in each striatal domain classified as each cell type. **d**, Averaged and smoothed firing rates (lines) and raster plots across trials (dots) for one example cell of each type in each domain, aligned to the indicated task event. Top row, DMS; middle row, DCS; bottom row, DLS. **e**, Waveform and autocorrelogram of unidentified interneurons (mean \pm s.d. across cells). **f**, Heat maps—spiking in individual cells aligned to contralateral stimuli (left), contralaterally orienting movements (middle) and rewards (right)—averaged across trials with reaction times less than 500 ms, maximum-normalized and sorted by time of maximum activity

using half of the trials and plotting the other half of trials, formatted as in Fig. 4b. Line plots, average activity across neurons, formatted as in Fig. 4c. **g**, Correlation of the activity of each neuron (rows within heat maps of **c**) with the average activity within cell types or cortical activity from a region of interest corresponding to each domain, calculated from nonoverlapping sessions to account for interneuron sparsity (mean \pm s.e. across sessions), formatted as in Fig. 4d. Unidentified interneurons were equally correlated to other unidentified interneurons, MSNs, FSIs and cortical activity (two-way ANOVA on firing rate and type, type $P=0.56$ across 77 sessions) and uncorrelated to TAN activity (two-way ANOVA on firing rate and type, type $P=2.7 \times 10^{-12}$ across 77 sessions). **h**, Activity during passive stimulus presentations in untrained (black) and trained (yellow) mice (mean \pm s.e. across sessions), activity increases in DMS and DCS (time window 0–0.2 s, rank-sum test, DMS: $P=5.5 \times 10^{-4}$, DCS: $P=1.4 \times 10^{-4}$ across 77 sessions).

Reporting Summary

Nature Research wishes to improve the reproducibility of the work that we publish. This form provides structure for consistency and transparency in reporting. For further information on Nature Research policies, see our [Editorial Policies](#) and the [Editorial Policy Checklist](#).

Statistics

For all statistical analyses, confirm that the following items are present in the figure legend, table legend, main text, or Methods section.

n/a Confirmed

- The exact sample size (n) for each experimental group/condition, given as a discrete number and unit of measurement
- A statement on whether measurements were taken from distinct samples or whether the same sample was measured repeatedly
- The statistical test(s) used AND whether they are one- or two-sided
Only common tests should be described solely by name; describe more complex techniques in the Methods section.
- A description of all covariates tested
- A description of any assumptions or corrections, such as tests of normality and adjustment for multiple comparisons
- A full description of the statistical parameters including central tendency (e.g. means) or other basic estimates (e.g. regression coefficient) AND variation (e.g. standard deviation) or associated estimates of uncertainty (e.g. confidence intervals)
- For null hypothesis testing, the test statistic (e.g. F , t , r) with confidence intervals, effect sizes, degrees of freedom and P value noted
Give P values as exact values whenever suitable.
- For Bayesian analysis, information on the choice of priors and Markov chain Monte Carlo settings
- For hierarchical and complex designs, identification of the appropriate level for tests and full reporting of outcomes
- Estimates of effect sizes (e.g. Cohen's d , Pearson's r), indicating how they were calculated

Our web collection on [statistics for biologists](#) contains articles on many of the points above.

Software and code

Policy information about [availability of computer code](#)

Data collection

Data analysis

For manuscripts utilizing custom algorithms or software that are central to the research but not yet described in published literature, software must be made available to editors and reviewers. We strongly encourage code deposition in a community repository (e.g. GitHub). See the Nature Research [guidelines for submitting code & software](#) for further information.

Data

Policy information about [availability of data](#)

All manuscripts must include a [data availability statement](#). This statement should provide the following information, where applicable:

- Accession codes, unique identifiers, or web links for publicly available datasets
- A list of figures that have associated raw data
- A description of any restrictions on data availability

Field-specific reporting

Please select the one below that is the best fit for your research. If you are not sure, read the appropriate sections before making your selection.

- Life sciences Behavioural & social sciences Ecological, evolutionary & environmental sciences

For a reference copy of the document with all sections, see [nature.com/documents/nr-reporting-summary-flat.pdf](https://www.nature.com/documents/nr-reporting-summary-flat.pdf)

Life sciences study design

All studies must disclose on these points even when the disclosure is negative.

Sample size	Sample sizes were chosen to be on par with similar studies using the least number of mice to establish robust results
Data exclusions	No data was excluded
Replication	Similar results were obtained across all mice, previous results were replicated in new cohorts for new experiments
Randomization	Mice were placed in cohorts according to which ones were ready at the time of each experiment
Blinding	Blinding was not relevant as we did not test manipulations across groups

Reporting for specific materials, systems and methods

We require information from authors about some types of materials, experimental systems and methods used in many studies. Here, indicate whether each material, system or method listed is relevant to your study. If you are not sure if a list item applies to your research, read the appropriate section before selecting a response.

Materials & experimental systems

n/a	Included in the study
<input checked="" type="checkbox"/>	<input type="checkbox"/> Antibodies
<input checked="" type="checkbox"/>	<input type="checkbox"/> Eukaryotic cell lines
<input checked="" type="checkbox"/>	<input type="checkbox"/> Palaeontology and archaeology
<input type="checkbox"/>	<input checked="" type="checkbox"/> Animals and other organisms
<input checked="" type="checkbox"/>	<input type="checkbox"/> Human research participants
<input checked="" type="checkbox"/>	<input type="checkbox"/> Clinical data
<input checked="" type="checkbox"/>	<input type="checkbox"/> Dual use research of concern

Methods

n/a	Included in the study
<input checked="" type="checkbox"/>	<input type="checkbox"/> ChIP-seq
<input checked="" type="checkbox"/>	<input type="checkbox"/> Flow cytometry
<input checked="" type="checkbox"/>	<input type="checkbox"/> MRI-based neuroimaging

Animals and other organisms

Policy information about [studies involving animals](#); [ARRIVE guidelines](#) recommended for reporting animal research

Laboratory animals	TetO-GCaMP6s;CaMKII-tTa transgenic mice, male and female over the age of 6 weeks
Wild animals	No wild animals
Field-collected samples	No field samples
Ethics oversight	The project was conducted under personal and project licenses from the UK Home Office

Note that full information on the approval of the study protocol must also be provided in the manuscript.